Characteristic Scales of Complexity and Coherence within Interplanetary Coronal Mass Ejections: Insights from Spacecraft Swarms in Global Heliospheric Simulations

Camilla Scolini [ID],[1, 2] Réka M. Winslow [ID],[1] Noé Lugaz [ID],[1] and Stefaan Poedts [ID][3, 4]

[1]Institute for the Study of Earth, Oceans, and Space, University of New Hampshire, Durham, NH, USA
[2]Cooperative Programs for the Advancement of Earth System Science (CPAESS), University Corporation for Atmospheric Research, Boulder, CO, USA
[3]Department of Mathematics/Centre for mathematical Plasma Astrophyics, KU Leuven, Belgium
[4]Institute of Physics, University of Maria Curie-Skłodowska, Lublin, Poland

ABSTRACT

Many aspects of the three-dimensional (3-D) structure and evolution of interplanetary coronal mass ejections (ICMEs) remain unexplained. Here, we investigate two main topics: (1) the coherence scale of magnetic fields inside ICMEs, and (2) the dynamic nature of ICME magnetic complexity. We simulate ICMEs interacting with different solar winds using the linear force-free spheromak model incorporated into the EUHFORIA model. We place a swarm of ~ 20000 spacecraft in the 3-D simulation domain and characterize ICME magnetic complexity and coherence at each spacecraft based on simulated time series. Our simulations suggest that ICMEs retain a lower complexity and higher coherence along their magnetic axis, but that a characterization of their global complexity requires crossings along both the axial and perpendicular directions. For an ICME of initial half angular width of $45°$ that does not interact with other large-scale solar wind structures, global complexity can be characterized by as little as 7–12 spacecraft separated by $25°$, but the minimum number of spacecraft rises to 50–65 (separated by $10°$) if interactions occur. Without interactions, ICME coherence extends for $45°$, $20°$–$30°$, $15°$–$30°$, and $0°$–$10°$ for B, B_ϕ, B_θ, and B_r, respectively. Coherence is also lower in the ICME west flank compared to the east flank due to Parker spiral effects. Moreover, coherence is reduced by a factor of 3–6 by interactions with solar wind structures. Our findings help constrain some of the critical scales that control the evolution of ICMEs and aid in the planning of future dedicated multi-spacecraft missions.

Keywords: Solar coronal mass ejections (310) — Solar wind (1534) — Interplanetary magnetic fields (824) — Corotating streams (314)

1. INTRODUCTION

Coronal mass ejections (CMEs; see e.g. Webb & Howard 2012) are large eruptions of plasma and magnetic field from the Sun into interplanetary space. When probed in situ by spacecraft crossing their structures, they are referred to as interplanetary CMEs (ICMEs; see e.g. Bothmer & Schwenn 1998; Cane & Richardson 2003; Kilpua et al. 2017a). ICMEs are among the largest and most energetic transients in the heliosphere, where they shape the space environment and can drive severe space weather disturbances at Earth and other planets (see e.g. Gosling et al. 1990; Tsurutani et al. 1992; Zhang et al. 2007; Kilpua et al. 2017b; Lee et al. 2017; Slavin et al. 2019; Winslow et al. 2020). ICMEs are characterized by a variety of in-situ signatures, with their core component being the so-called magnetic ejecta (ME; Winslow et al. 2015), i.e. a region of enhanced magnetic field corresponding to the original structure erupted at the

Corresponding author: Camilla Scolini
camilla.scolini@unh.edu

Sun, which may or may not be preceded by a forward shock and a turbulent sheath formed during propagation (Kilpua et al. 2017a). The entire propagating structure, composed of the ME and its associated shock and sheath (if present) is referred to as the ICME. We use the term ME as a more general term than magnetic cloud, which follows the strict definition of Burlaga et al. (1981). Typically, MEs are associated with a low plasma β ($\ll 1$) near 1 au, indicating that the magnetic pressure dominates over the thermal pressure and that their internal dynamics and 3-D structure are controlled primarily by magnetic forces. MEs also often exhibit rotations in the magnetic field components, which are compatible with a configuration of magnetic field bundles twisting around a central axis (Burlaga 1988; Lepping et al. 1990; Kilpua et al. 2017a). This has led to the proliferation of flux-rope (FR) models to describe the ME local and global magnetic structure (see, e.g., Lepping et al. 1990; Mulligan & Russell 2001; Marubashi & Lepping 2007; Hidalgo & Nieves-Chinchilla 2012; Hidalgo 2013; Isavnin 2016; Nieves-Chinchilla et al. 2016, 2018a; Weiss et al. 2021). FR models have also been successful in describing the CME pre-eruptive and eruptive configuration, early evolution in the solar corona, and interplanetary evolution up to Mars and beyond (e.g. Vourlidas 2014; Patsourakos et al. 2020; Palmerio et al. 2021; Davies et al. 2022).

ICMEs evolve significantly as they propagate through the solar wind. In particular, interactions with other large-scale interplanetary structures such as high speed streams (HSSs; Cranmer et al. 2017), stream interaction regions (SIRs; Richardson 2018), or other ICMEs can induce dramatic changes to ICME structures (Manchester et al. 2017; Lugaz et al. 2017). Therefore, understanding the effect of different propagation scenarios on ICMEs is necessary to characterize their evolution across a wide range of spatial and temporal scales. To this end, recent studies have explored the changes in magnetic complexity (i.e., the degree of similarity/deviation from an ideal FR configuration) that MEs can undergo during propagation. In-depth investigations of MEs observed by radially-aligned spacecraft provided ample evidence that MEs evolve and tend to increase their magnetic complexity during propagation through interplanetary space, primarily due to interaction with other large-scale solar wind structures (Mulligan et al. 1999; Nieves-Chinchilla et al. 2012; Good & Forsyth 2016; Winslow et al. 2016, 2021b,a). Scolini et al. (2022) provided further statistical support to these results through an investigation of 31 MEs observed in radial alignment between Mercury and 1 au. Furthermore, Scolini et al. (2021b) conducted a numerical investigation of the probability of detecting a complexity increase between an inner and outer spacecraft in perfect radial alignment, finding that the interaction with HSSs and SIRs doubles the probability for an MEs to undergo complexity changes. To date it has not been possible to completely characterize the spatial (i.e. longitudinal and latitudinal) magnetic complexity distribution of MEs and its evolution with heliocentric distance due to the limited number of spacecraft crossing individual ME structures.

Direct probing of ICMEs relies on in situ spacecraft measurements obtained at a given location in space (i.e. along a 1-D trajectory). However, single-point measurements only provide information on the local properties of an ICME at a particular stage of its evolution, and it remains unclear to what extent they are indicative of their global structure (e.g. Möstl et al. 2012; Al-Haddad et al. 2013, 2018; Marubashi & Cho 2015; Lugaz et al. 2018). Multi-point observations at the same heliocentric distance but at different locations in space represent the best opportunity to probe the 3-D structure of ICMEs at a given stage of their evolution, as they allow for a direct probing of the in situ ICME characteristics at multiple locations while mitigating the effect of local variations (e.g. Möstl et al. 2012; Weiss et al. 2021). However, these remain relatively scarce, as the majority of ICMEs are still probed in situ by single spacecraft, and the maximum number of spacecraft crossings at a given heliocentric distance per individual event is limited to three (e.g. Burlaga et al. 1981; Mulligan & Russell 2001; Kilpua et al. 2011; Lugaz et al. 2022). Additionally, such measurements have so far been obtained only near 1 au, either by multiple spacecraft in L1 orbits (at small angular separations $\leq 1°$), or for spacecraft angular separations above $10°$, with other heliocentric distances and critical scales around $1° - 10°$ remaining unprobed (Lugaz et al. 2018).

Prominent open questions related to the 3-D nature of ICMEs are whether their MEs are magnetically coherent objects, and at what spatial scales such a coherence exists. Strictly speaking, magnetic coherence within an ME refers to its ability to respond to external perturbations in a coherent (i.e. solid-like) manner (Owens et al. 2017). Coherent behavior requires information to propagate across an ME structure, and magnetic forces to be sufficiently strong to resist external deformation forces (Owens et al. 2017). Following an analytical approach based on the consideration of expansion and Alfvén speeds within MEs at 1 au, Owens et al. (2017) and Owens (2020) estimated an upper limit for the angular scale of magnetic coherence to $\sim 26°$, which is significantly smaller than the typical angular width of MEs (around $40° - 60°$; e.g. Yashiro et al. 2004; Kilpua et al. 2011; Good & Forsyth 2016). From an observational standpoint, the correlation of magnetic field components among different locations within an ME has been regarded

as a proxy for magnetic coherence (Matsui et al. 2002; Farrugia et al. 2005; Lugaz et al. 2018; Ala-Lahti et al. 2020), although it remains unclear how the ability of information to propagate across an ME affects its local properties, and how this relates to the ability of the same ME to use such information in order to resist deformation by external factors and behave as a coherent structure (Owens 2020). The investigation by Lugaz et al. (2018) across various angular separations pointed towards the potential existence of two characteristic scales of correlation within MEs near 1 au: one related to the magnetic field components (around $4°$–$7°$) and one for the total magnetic field (around $14°$–$20°$). Yet, limitations on the data available prevented the exploration of the whole parameter space, particularly at scales between $1°$ and $10°$.

It remains extremely challenging to answer some of the most fundamental questions on the nature of MEs, particularly with respect to their magnetic complexity and coherence and their evolution with heliocentric distance. In this paper, we address these topics by turning to numerical simulations and exploiting their 3-D capabilities to investigate the following science questions: (1) What is the spatial distribution of magnetic complexity within MEs? (2) Across what spatial scales could MEs behave as magnetically coherent objects? (3) How does all of the above depend on the heliocentric distance and the specific propagation history of an ME, such as its interaction with other large-scale solar wind structures? We address the aforementioned questions by means of global heliospheric simulations performed with the EUropean Heliospheric FORecasting Information Asset (EUHFORIA; Pomoell & Poedts 2018), using idealized solar wind set-up as in Scolini et al. (2021b) and simulating CMEs/MEs using a linear force-free spheromak model (Verbeke et al. 2019). This work represents the first-ever attempt to specifically address the problem of magnetic coherence by analyzing numerical simulation results using techniques typically employed in the analysis of in situ observations.

The paper is structured as follows. In Section 2, we introduce the numerical model and the methods used to investigate the magnetic complexity and coherence of MEs using global heliospheric simulations. In Section 3, the analysis of two simulations considering different interaction scenarios between an ME and the surrounding solar wind is presented, and results are discussed with respect to baseline values obtained for a stand-alone ideal spheromak magnetic structure, and to the propagation history of each ME. In Section 4, we examine possible implications of our results for future dedicated multi-spacecraft missions orbiting close to the ecliptic plane. Finally, in Section 5, we summarize our conclusions and outlook.

2. METHODS

2.1. *Numerical Set-Up*

In this work, we build on the analysis of the numerical simulations previously presented by Scolini et al. (2021b), that were performed using the EUHFORIA 3-D magnetohydrodynamic (MHD) model of the inner heliosphere (Pomoell & Poedts 2018). To evaluate the interaction of ICMEs with different solar wind structures, two background solar wind configurations are simulated: the first one (hereafter "run A") includes a uniform solar wind of speed 450 km s^{-1} except for a low-inclination heliospheric current/plasma sheet (HCS/HPS). The second one (hereafter "run B") differs from the one above by having a more highly inclined HCS/HPS, and by the inclusion of a HSS of radial speed equal to 675 km s^{-1} and circular cross-section of half angular width equal to $30°$. In both cases, the HPS meridional profile is parametrized using the description in Odstrčil et al. (1996), resulting in a solar wind speed as low as 300 km s^{-1} near the HCS. This choice has been made to ensure full control over the ICME propagation and interaction with solar wind structures, and the comparability between different runs. In the two runs, CMEs are initialized as linear force-free spheromak structures as described by Verbeke et al. (2019), with the following set of geometric, kinematic, and magnetic parameters: radial speed equal to $v_R = 800$ km s^{-1}; initial half angular width of $\omega/2 = 45°$; positive chirality ($H = +1$) with axial tilt $\gamma = 90°$ with respect to the northward direction (corresponding to a SWN flux-rope type; see Bothmer & Schwenn 1998); toroidal magnetic flux (φ_t) equal to 10^{14} Wb (corresponding to a magnetic field strength of ~ 25 nT at 1 au). Because of the pressure imbalance between the CME and the surrounding solar wind upon insertion in the heliospheric domain (leading to an expansion of the CME structure, as shown by Scolini et al. 2019, 2021a), the effective initial CME front speed is ~ 1100 km s^{-1}, which results in a fast CME that drives an interplanetary shock and sheath. Such a combination of initial parameters is representative of those of a typical fast CME with a reconnected flux of the order of 10^{14} Wb (Pal et al. 2018). The CME initial direction is chosen to reproduce two end-member scenarios of interaction with different solar wind structures: in run A, the CME is inserted across the HCS/HPS at $(\theta, \phi) = (0°, 0°)$; in run B, the CME is inserted across the HSS at $(\theta, \phi) = (5°, 0°)$, in a configuration similar to that of CMEs originated from "anemone" active regions (e.g. Lugaz et al. 2011; Sharma & Cid
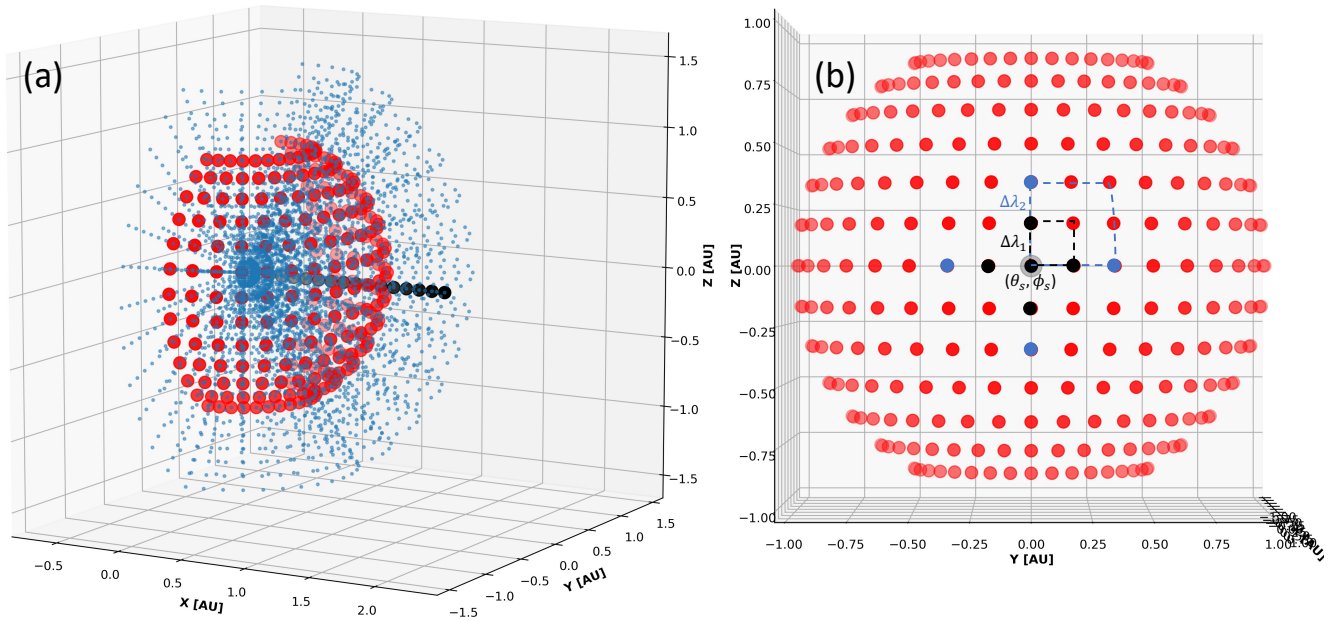
Figure 1. Spatial distribution of the spacecraft swarm used in EUHFORIA simulations. (a): Angled view showing the global distribution of virtual spacecraft in 3-D space (in blue). Red dots indicate the virtual spacecraft located at 1 au. Black dots mark the virtual spacecraft located along the CME initial direction. (b): Front view showing only the virtual spacecraft at 1 au. For a reference spacecraft serving as seed location (θ_s, ϕ_s), the re-binning of ME types with nearby spacecraft for two different $\Delta\lambda$ values is indicated by the dashed polygons. For the same reference spacecraft, first neighbors considered under the rook criterion employed to determine the Moran's I coefficient, for two different $\Delta\lambda$, are indicated as black and blue colored dots.

2020). The CME insertion time is arbitrarily set on January 1, 2020 at 00:00 UT. A detailed discussion of the model set-up is available in Scolini et al. (2021b).

Our simulation domain expands from 0.1 to 2.0 au in the radial direction (r), covering $\pm 80°$ in the latitudinal direction (θ), and $\pm 180°$ in longitude (ϕ), with a uniform grid composed of $512(r) \times 80(\theta) \times 180(\phi)$ cells. In our simulation domain, we place a set of virtual spacecraft where the time-dependent MHD parameters are extracted in a similar way to that done by real spacecraft monitoring the in situ plasma conditions in space. Virtual spacecraft are placed at longitudinal and latitudinal separations of $\Delta\lambda = 5°$, spanning $\pm 90°$ in longitude from the CME initial direction, and covering the full range of latitudes in the simulation domain. They are also uniformly distributed in the radial direction between 0.11 and 1.61 au (i.e., from the model inner boundary to the orbit of Mars) with a 0.1 au radial separation. Overall, a swarm of 18944 virtual spacecraft (1184 per heliocentric distance) is placed in the model domain in each simulation. Each virtual spacecraft records time profiles of the standard MHD output in EUHFORIA: the velocity vector, magnetic field vector, density, and thermal pressure in Heliocentric Earth Equatorial (HEEQ) coordinates. Figure 1 (a) provides a global view of the locations of the virtual spacecraft considered, while a detailed discussion about their use in this paper's analysis is provided in the following sections.

2.2. *Metrics of Magnetic Complexity*

Time-dependent information on the MHD variables (i.e. velocity vector, magnetic field vector, density, and thermal pressure in HEEQ coordinates) at each simulated spacecraft are used to investigate the spatial and temporal evolution of the magnetic complexity characterizing the simulated ICMEs, and particularly their ME structures, as described below.

2.2.1. *Frequency of Magnetic Ejecta Types*

At each virtual spacecraft located at coordinates (r, θ, ϕ) in the simulation domain, we identify whether an ME signature is present in the simulated time series using the identification scheme provided in Scolini et al. (2021b). This classification scheme considers the magnetic field and plasma β to identify the presence or absence of an ME following a preceding interplanetary shock, and to determine its front and rear boundaries. The preceding shock is identified

based on jump conditions on the radial speed, density, and magnetic field. If an ME is detected, we characterize its complexity based on the maximum rotation detected in the magnetic field components by using the classification scheme previously introduced by Scolini et al. (2021b) and based on previous observational works by Nieves-Chinchilla et al. (2018b, 2019). Our classification differs from the one by Nieves-Chinchilla et al. (2018b, 2019) in the fact that it is adapted to reflect the full range of rotation angles expected to be observed when crossing a spheromak structure, ranging between 0° and 360° as detailed by Scolini et al. (2021b). In summary, each ME signature is classified as F_{270}, F_{180}, F_{90}, F_{30} or E when at least one component (i.e. B_R, B_T, or B_N) rotates by $\geq 270°$, $\geq 180°$, $\geq 90°$, $\geq 30°$, or $< 30°$, respectively. Additionally, we assign a numerical index, defined as "complexity index" ($\mathbb{C}$), to each ME class detected in situ, in order to rank the level of complexity of the detected structure: $\mathbb{C} = 0$ for F_{270} class, $\mathbb{C} = 1$ for F_{180} class, $\mathbb{C} = 2$ for F_{90} class, $\mathbb{C} = 3$ for F_{30} class, and $\mathbb{C} = 4$ for E class. As a result, a complexity scale between 0 and 4 is defined, with higher complexity values indicating higher deviations from the FR signatures expected for an ideal spheromak, which exhibit rotations larger than 270° for most crossings near the spheromak central axis (see Figure 6 in Scolini et al. 2021b). Additionally, a value of $\mathbb{C} = 5$ is assigned to shock-only ICME signatures, while $\mathbb{C} = 6$ is assigned to all spacecraft locations that did not detect any ICME-related signature. Example signatures for each ME class are provided in the appendix of Scolini et al. (2021b). We note this definition of complexity is solely based on the magnetic field signatures associated with a given ME, and it does not take into account any plasma information nor the properties of its preceding shock and sheath. This choice was made to be consistent with observational works in the past ~ 15 years, which could only make use of magnetic field data at distances other than 1 au (Winslow et al. 2016, 2021b; Scolini et al. 2022; Davies et al. 2022). However, it will be important for future investigations of ICME complexity to asses them holistically, i.e., by looking at changes in all aspects of the ICME as opposed to just the magnetic parameters within the ME, to understand complexity changes from a more fundamental standpoint.

In our simulation runs A and B, the frequency of ME types detected at different spacecraft is then investigated as a function of the heliocentric distance, and of the angular separation $\Delta\lambda$ of the simulated spacecraft crossing through the ME structure. To explore different spatial scales, we resample the initial spacecraft distribution (uniformly separated in longitude and latitude by $\Delta\lambda = 5°$) to progressively larger $\Delta\lambda$, covering $\Delta\lambda$ between 5° and 45°. After defining a "seed" location (θ_s, ϕ_s) corresponding to the reference location for the resampling of the spacecraft distribution, spacecraft located between $(\theta_s + n\Delta\lambda, \phi_s + m\Delta\lambda)$ and $(\theta_s + (n+1)\Delta\lambda, \phi_s + (m+1)\Delta\lambda)$ are binned into the n-th (m-th) bin of the new spatial distribution in latitude (longitude). A representation of such a re-binning process is provided in Figure 1 (b). Information from individual spacecraft binned within the same $\Delta A = \Delta\lambda \times \Delta\lambda$ areal unit is then combined by taking the mode of the ME type distribution across ΔA, which corresponds to the most probable ME class that would be observed by a spacecraft crossing anywhere within ΔA.

Because results expressed in terms of $\Delta\lambda$ also depend on the specific CME half angular width ($\omega/2$) prescribed at insertion through the domain inner boundary, we also express angular separations as fractions of the CME initial half angular width ($F_{\omega/2}$, ranging between 0 and 1), which are independent of the prescribed CME half angular width and can therefore be extrapolated to CMEs of different sizes. When relevant, the associated number of virtual spacecraft crossing the ME structure is also reported.

In the following, we consider the occurrence of ME types detected at different spacecraft to provide a global measure of ME magnetic complexity: the lowest the $\mathbb{C}$ values detected within an ME, the lowest its global complexity. Furthermore, we identify the characteristic scale of magnetic complexity as the maximum angular separation $\Delta\lambda$ at which spacecraft are able to detect the same two most frequent ME classes detected by spacecraft with minimum $\Delta\lambda = 5°$ separation, at all heliocentric distances. We clarify this choice in the identification of the characteristic scale of magnetic complexity in Sections 3.1 and 3.2, when discussing the results for an ideal spheromak structure and for a spheromak propagating through a quiet solar wind.

2.2.2. *Spatial Autocorrelation of Magnetic Ejecta Types: the Moran's I*

To evaluate how ordered is the spatial distribution of ME complexity at each heliocentric distance r considered, we use the Moran's I (Moran 1950) as a measure to quantify the spatial autocorrelation (i.e. the presence of systematic spatial variation in a certain variable) of different ME types detected within the simulated ICMEs. The Moran's I at a given heliocentric distance r is defined as

$$I(r) = \frac{N}{W} \frac{\sum_{i=1}^{N} \sum_{j=1}^{N} w_{ij}(x_i - \bar{x})(x_j - \bar{x})}{\sum_{k=1}^{N}(x_k - \bar{x})^2}, \tag{1}$$

where N is the total number of spacecraft observations at a given heliocentric distance r; $x_i = \mathbb{C}_i$ is the value of the ME complexity index at a given location i corresponding to coordinates (r, θ_i, ϕ_i); $x_j = \mathbb{C}_j$ is the value of the ME complexity index at a location j corresponding to coordinates (r, θ_j, ϕ_j); and $\bar{x} = \bar{\mathbb{C}}$ is the mean of all $x_i = \mathbb{C}_i$ values, for $i = 1, ..., N$. The contiguity between two spatial units is assessed using the rook criterion, which takes as neighbors any pair of spacecraft that are aligned in longitude or latitude (i.e. whose location cells on a grid share an edge). For the specific spacecraft swarm configuration used in this work's simulations, the neighbors of a given spacecraft using the rook criterion are indicated by the blue and black colored dots in Figure 1 (b) for two different $\Delta\lambda$ values. w_{ij} is the weight of location i relative to j, and it assumes a value of 1 for pairs of spacecraft that are aligned in longitude or latitude, and a value of 0 for pairs of spacecraft that are diagonally aligned. W is the sum of all weights w_{ij} over the set of N locations considered. Under such a prescription, a Moran's $I(r)$ close to 1 indicates a well-ordered, highly-clustered spatial distribution of ME types and is taken as indication of the lowest complexity state possible for an ME magnetic structure; a Moran's $I(r)$ approaching 0 indicates a random arrangement of ME types in space, and therefore indicates the highest complexity state. In the following, we consider $I > 0.5$ as indicative of a low-complexity, highly clustered spatial distribution of ME classes within an ME, and $I \leq 0.5$ as indicative of a high-complexity, randomly-arranged distribution.

Similarly to the occurrence of ME types, we compute the Moran's I for different spacecraft separations $\Delta\lambda$, and we evaluate its changes as a function of the heliocentric distance to assess the role of interactions between ICMEs and solar wind structures in randomizing the internal magnetic field of MEs. The Moran's I for different spatial scales is obtained from the resampled spatial distribution of the complexity index $\mathbb{C}$, as described in Section 2.2.1. In addition to the occurrence of ME classes discussed in Section 2.2.1, we use the Moran's I as a complementary global metric to quantify the degree of complexity within an ME.

2.2.3. *Spatial Autocorrelation of Magnetic Ejecta Types: the Local Moran's I*

To gain information on the local properties of ME complexity, we further inspect the spatial distribution of magnetic complexity through the Local Moran's I (also known as Anselin's Local Indicator of Spatial Association; Anselin 1995). This metric corresponds to the local formulation of the Moran's I, which is calculated locally for each areal unit in the data spatial distribution. Specifically, the Local Moran's I at a given location (r, θ_i, ϕ_i) is defined as

$$I_i(r) = (x_i - \bar{x}) \sum_{j=1}^{N_i} w_{ij}(x_j - \bar{x}), \tag{2}$$

where N_i is the number of neighboring spacecraft observations to the reference location i corresponding to coordinates (r, θ_i, ϕ_i); $x_i = \mathbb{C}_i$ is the ME complexity index at location i; $x_j = \mathbb{C}_j$ is the ME complexity index at location j corresponding to coordinates (r, θ_j, ϕ_j) neighboring location i; and $\bar{x} = \bar{\mathbb{C}}$ is the mean of all $x_j = \mathbb{C}_j$ neighboring values of location i, for $j = 1, ..., N_i$. As for Equation 1, w_{ij} is the weight of location i relative to j, as determined by the rook criterion.

With respect to the specific problem considered in this work, the Local Moran's I proves particularly useful to investigate the spatial distribution of ME complexity as a function of the heliocentric distance, and to quantify to what degree interactions with interplanetary structures affect the magnetic complexity in different regions of an ME. In particular, to locate the source of complexity changes, we track the (θ, ϕ) location of the maximum of the Local Moran's I ($\max(I_i)$) with heliocentric distance, and relate it to the conditions of the surrounding solar wind along the corresponding propagation direction.

2.3. *Metrics of Magnetic Coherence*

As previously done for magnetic complexity, we consider time-dependent information on the MHD plasma variables at each simulated spacecraft to investigate the spatial and temporal evolution of the magnetic coherence characterizing the simulated ICMEs, and particularly their ME structures, as described below. Our final aim is to characterize the spatial properties and scale of ME magnetic coherence and its evolution depending on the characteristics of the solar wind encountered by an ICME along its journey through the heliosphere.

2.3.1. *Scale of Magnetic Coherence: Correlation of Magnetic Field Profiles at Different Spacecraft*

In the following, we investigate ME magnetic coherence in a similar manner as previous observational investigations, i.e. by quantifying the spatial scales at which the time series of the components and magnitude of the magnetic field
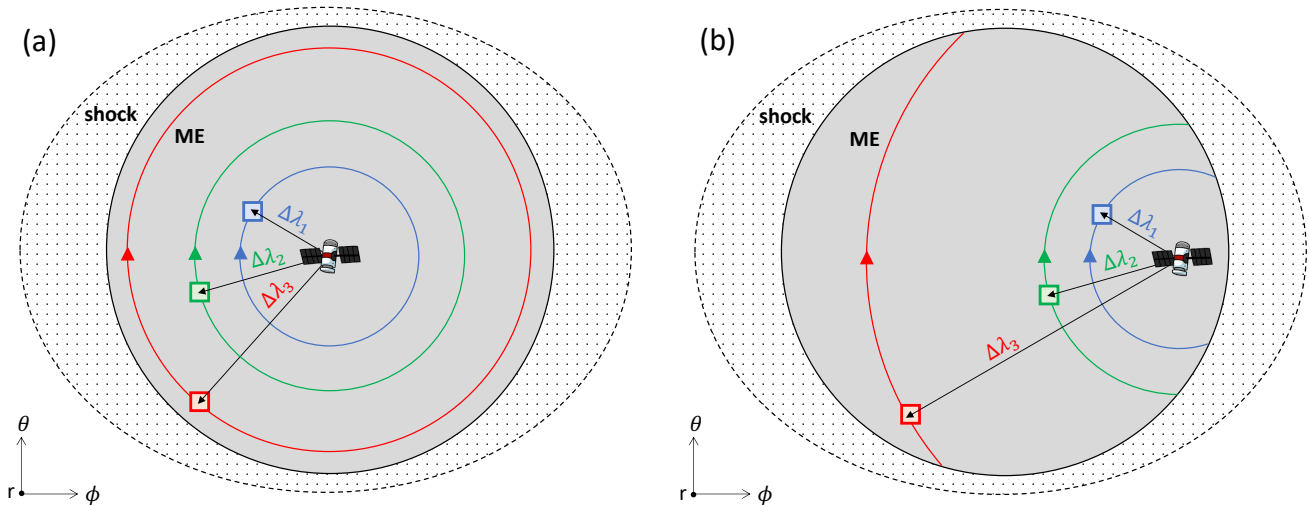
Figure 2. Sketch of the methodology used to determine the average correlation scale of the magnetic field profiles around a reference observer crossing through the ME center (a) and west (b) region. Different angular scales ($\Delta\lambda_i$) are indicated in different colors. The ICME is plotted as propagating heads on towards the observer.

within simulated MEs exhibit high levels of correlation. To achieve our goal, for each heliocentric distance r, we assess the correlation of the magnetic field profile measured within the ME at each spacecraft location (r, θ_i, ϕ_i) with respect to selected reference positions $(r, \theta_{\rm ref}, \phi_{\rm ref})$. We then compute average correlations across all spacecraft located at a given angular separation from the reference spacecraft $(\Delta\lambda)$, i.e. by taking the average along all directions around the reference location, for different angular separations. By comparing the average correlations obtained at different angular separations, we determine the maximum angular separation at which two spacecraft are likely to observe correlated time profiles for a given magnetic field component. As correlation scales around a given reference spacecraft may be anisotropic along different directions, the correlation scale for a given magnetic field component is estimated by averaging across different directions around the reference observer and chosen as the maximum angular separation at which correlation coefficients are ≥ 0.6 on average. Cartoons describing its derivation by averaging across different directions with respect to two different reference observers, one crossing near the center of the ME and one near its west flank, for three given angular separations $\Delta\lambda$, are provided in Figure 2 (a) and (b), respectively. We note that our definition of correlation scale is different from those used by Lugaz et al. (2018) and Wicks et al. (2010) to investigate the ME and solar wind correlation lengths from in situ measurements. A justification on the different definition chosen in this study compared to previous studies on spatial correlations is provided in Section 3.4, when discussing the results for spheromaks propagating through different solar winds with respect to the baseline model consisting of an ideal spheromak structure.

3. RESULTS FOR SPHEROMAK STRUCTURES PROPAGATING IN THE HELIOSPHERE

In this section, we explore the evolution of magnetic complexity and coherence within MEs propagating through different solar winds in EUHFORIA, and we discuss how deviations from the patterns retrieved for an ideal spheromak structure depend on the characteristics of the interaction with the surrounding solar wind. In light of the results by Scolini et al. (2021a,b), we focus our discussion on heliocentric distances between 0.3 au and 1.6 au and neglect results between 0.1 au and 0.3 au, where ICME over-expansion and challenges in the determination of the ME boundaries from simulated time series in the early stage of the ICME propagation might have otherwise influenced our results and conclusions. As a caveat to the interpretation of the results, we note that the chosen numerical set-up ensures more control over the various propagation effects affecting different ICME regions during propagation compared to performing simulations of real ICME events propagating through a magnetogram-extrapolated solar wind. The insertion of a perfectly-known global CME magnetic structure at the inner boundary of the heliospheric domain (located at 0.1 au in our simulations) also ensures enhanced control over the evolution of its magnetic structure, facilitating our interpretation of propagation effects. However, it is important to acknowledge that such an approach will likely result in a more regular/smooth magnetic configuration in simulated ICMEs compared to real ICMEs at the same

heliocentric distance. To avoid drawing inappropriate conclusions, in the following we put care into the interpretation of EUHFORIA results with respect to a baseline model (i.e. a stand-alone ideal spheromak model).

3.1. Baseline Results: Complexity and Coherence in an Ideal Spheromak Structure

We start discussing the results of our investigation by summarizing the baseline values obtained from the consideration of an ideal, stand alone spheromak structure. Characterizing the baseline level of complexity and coherence in such an idealized condition represents a first but necessary step to later be able to conduct a meaningful interpretation of the results obtained for spheromak structures propagating through different solar wind conditions.

As a first global measure of ME magnetic complexity considered, we report the frequency of detection of different ME classes as a function of the angular separation of the spacecraft crossings in the ideal spheromak. We find that for spacecraft separations of $\Delta\lambda = 5°$, about 80% of the detections are F_{270} (corresponding to $\mathbb{C} = 0$) and F_{30} (corresponding to $\mathbb{C} = 3$), which therefore contribute the most to the overall complexity of the ME. This result justifies our choice of considering only the two most frequently detected ME types as metrics of global ME complexity, and it applies also to simulated spheromaks propagating through different ambient solar winds, as discussed in Section 3.2. On the other hand, less represented ME classes (i.e. F_{180}, F_{90}, and E types, corresponding to $\mathbb{C} = 1, 2$, and 4, respectively) are observed by less than 10% of the spacecraft and quickly disappear as soon as the spacecraft angular separation becomes $\Delta\lambda \sim 15°$ ($F_{\omega/2} \sim 0.33$) or larger. For increasing spacecraft angular separations, we find that $\Delta\lambda = 25°$ (corresponding to $F_{\omega/2} \sim 0.55$ of the CME half angular width) is the maximum separation that guarantees a characterization of the magnetic complexity of the ideal spheromak as good as a $\Delta\lambda = 5°$ separation in terms of the two most frequently observed ME classes (i.e. F_{270} and F_{30} types).

The second global measure of ME magnetic complexity considered in this work is the Moran's I. The Moran's I is around 0.95 for angular separations $\Delta\lambda = 5°$ ($F_{\omega/2} = 0.11$), and it decreases at larger angular scales. The decrease of I for increasing $\Delta\lambda$ reflects the uncorrelated nature of ME signatures detected by spacecraft crossing the ME trajectories far apart. Overall, a spheromak structure exhibits a highly clustered spatial distribution of ME classes ($I \geq 0.5$, indicating a low complexity) when observed at scales $\Delta\lambda \lesssim 25°$ (corresponding to $F_{\omega/2} \lesssim 0.55$), and a more randomly-arranged ME type distribution ($I < 0.5$, indicating a high complexity) at scales $\Delta\lambda = 25° - 45°$ (corresponding to $F_{\omega/2} = 0.55 - 1$).

Finally, as a proxy for the coherence of an ME, we consider the average correlation scales of the magnetic field profiles around three reference observers crossing near the east, center, and west portion of the ME structure. We find that B, B_θ and B_ϕ show high correlations throughout the spheromak structure for all the observers considered, while the spatial correlation pattern for B_r appears highly variable depending on the reference location considered, resulting in much smaller correlation scales ($\Delta\lambda \sim 0° - 25°$ depending on the observer). While the exact characteristics of such a pattern are specific to the spheromak model considered in this study, a lower correlation in B_r than in the remaining magnetic field components has also been reported in actual observations (Lugaz et al. 2018) and by simple geometrical considerations, is expected to affect other flux rope models as well for observers crossing along different trajectories.

3.2. Characteristic Scales of Magnetic Complexity during Propagation

In what follows, we discuss the simulation results for EUHFORIA runs A and B with regards to scales of magnetic complexity as the ICME evolves during propagation. Figure 3 shows the frequency of detection of different ME classes recovered by virtual spacecraft crossing the MEs through different trajectories in EUHFORIA runs A and B, as a function of the heliocentric distance. Figure 3 (a) shows that for an ICME propagating through a quiet, quasi-uniform solar wind (run A) and observed by spacecraft at 5° separation, about 70% of all detections are F_{270} or F_{30} ME classes (corresponding to $\mathbb{C} = 0$ and 3, respectively), which therefore contribute the most to the overall complexity of the ME. This remains true for all heliocentric distances sampled. This result applies not only to a spheromak propagating through a quasi-uniform solar wind, but also to a stand-alone ideal spheromak structure (see Section 3.1), and it justifies our choice of considering only the two most frequently detected ME types as metrics of global ME complexity. Based on this result, we consider a given angular scale $\Delta\lambda$ (or the corresponding $F_{\omega/2}$) to provide a good representation of the global magnetic complexity of an ME structure when the two ME classes most frequently detected are well represented for all heliocentric distances.

The remaining three classes, i.e. F_{180}, F_{90} and E (corresponding to $\mathbb{C} = 1, 2$ and 4, respectively), are more rarely detected (each between 0% and 20%, depending on the heliocentric distance). This ranking is well represented up to $\Delta\lambda = 25°$ (Figure 3 (b)–(e)), while at larger separations, the ranking between most and least frequently observed
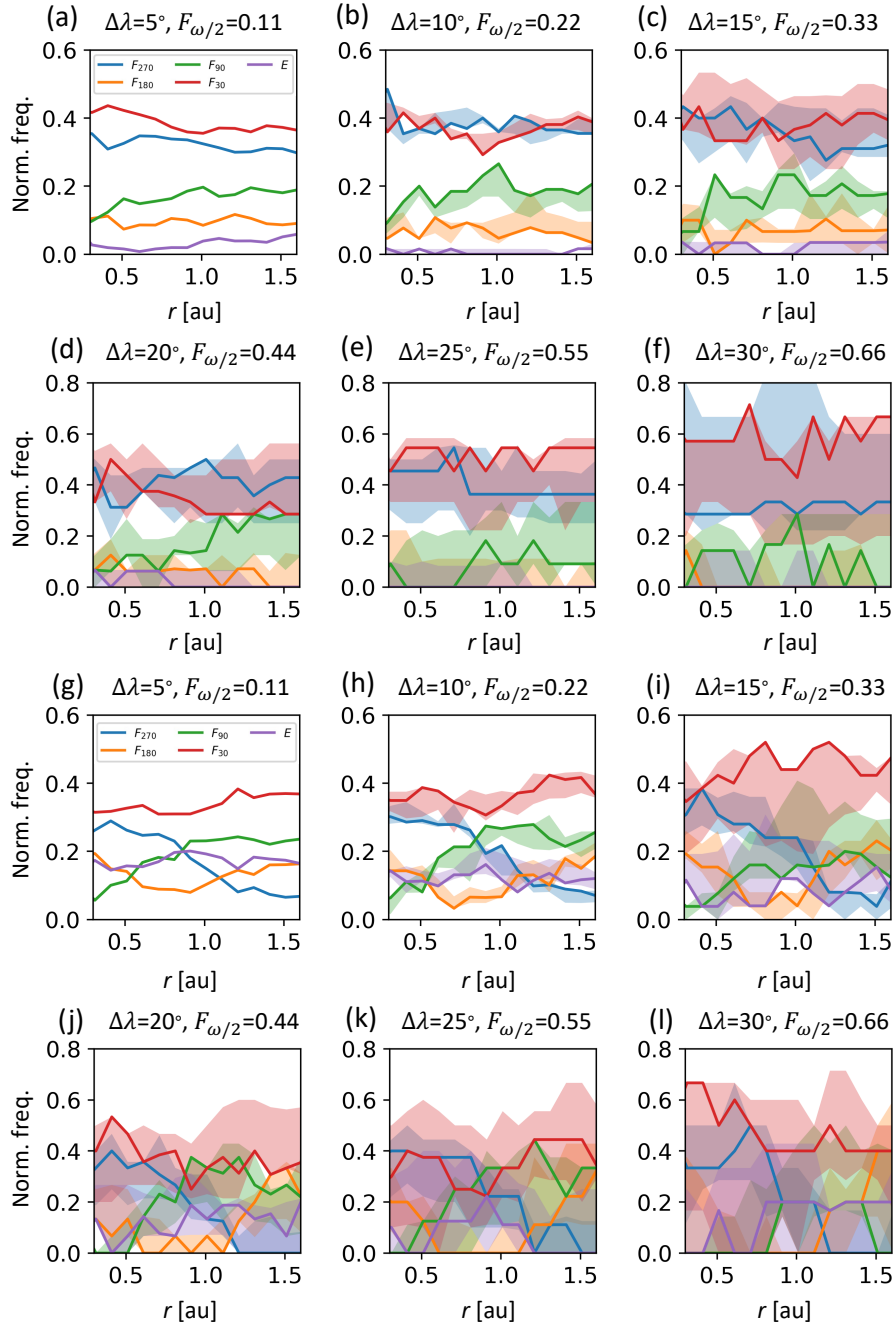
Figure 3. Normalized frequency of ME types detected as a function of the heliocentric distance and of the spacecraft angular separation, for the two CMEs simulated in EUHFORIA. (a)–(f): results for run A. (g)–(l): results for run B. Different panels show the results for different spacecraft separation considered. In all panels, the continuous lines indicate the results for a seed location at $(\theta_s, \phi_s) = (0°, 0°)$, while the shaded areas indicate the uncertainty (i.e. the spread, corresponding to the range of maximum and minimum values) as obtained by picking 20 random seed locations.

classes is significantly altered depending on the seed location chosen (Figure 3 (f)). We therefore conclude that the maximum $\Delta\lambda$ guaranteeing a good representation of the ME global magnetic complexity and its evolution with heliocentric distance is about 25° for the case without interactions with other structures. This corresponds to about 7 to 12 observing spacecraft, and to spatial scales equal to $F_{\omega/2} = 0.55$ of the initial CME half angular width. Such

scales, as well as the occurrence of different ME types detected within the ME, are both comparable to the results retrieved from the analysis of an ideal spheromak structure (as discussed in Section 3.1), indicating that the magnetic complexity of an ME within an ICME propagating through a quasi-uniform solar wind remains approximately constant during propagation, and at all times similar to the one of a pristine structure.

In contrast, the distribution of ME classes is highly variable with heliocentric distance when interactions occur. Figure 3 (g) shows that in the case of an ICME interacting with a preceding HSS/SIR (run B) and observed by spacecraft at 5° separation, results are similar to run A only up until 0.9 au, with the two dominant ME classes being F_{270} ($\mathbb{C} = 0$) and F_{30} ($\mathbb{C} = 3$). At larger heliocentric distances, the second most frequently detected ME type changes from F_{270} to the more complex F_{90} type ($\mathbb{C} = 2$). This indicates that the ME increases its global complexity during propagation as a consequence of the interaction with the HSS/SIR (consistent with previous findings by e.g. Winslow et al. 2016, 2021b; Scolini et al. 2021b, 2022). Additionally, the ranking between most and least frequently observed classes is well represented only up to spacecraft separations of $\Delta\lambda = 10°$ (Figure 3 (h)), while at larger separations it varies depending on the seed location chosen (Figure 3 (i) to (l)). We conclude that the distribution of ME types, and therefore of ME complexity as a whole, requires observations by about 50 to 65 spacecraft, separated by about $F_{\omega/2} = 0.22$ of the initial CME half angular width. In this case, the characteristic scale necessary to capture ME complexity is less than half of the scale retrieved from the analysis of an ideal spheromak structure (see Section 3.1), and of an ME not undergoing any interactions. This highlights that smaller angular separations must be used when investigating magnetic complexity within an ME that interacts with other large-scale structures compared to ICMEs that propagate through a quasi-uniform, quiet solar wind.

3.3. *Spatial Autocorrelation of Magnetic Complexity: Evolution of the Moran's I during Propagation*

Next, we investigate the spatial distribution of magnetic complexity within the modeled MEs by considering the Moran's I evolution with heliocentric distance. In run A (non-interacting ICME), the Moran's I decreases with increasing $\Delta\lambda$ but is essentially unchanged during propagation towards larger heliocentric distances (Figure 4 (a)). At 0.3 au, the range covered by the Moran's I lies between $0.93^{+0.00}_{-0.00}$ for $\Delta\lambda = 5°$ and $\sim 0.30^{+0.01}_{-0.22}$ for $\Delta\lambda = 45°$, which is very similar to values at 1.6 au (between $0.90^{+0.00}_{-0.00}$ for $\Delta\lambda = 5°$ and $\sim 0.30^{+0.06}_{-0.19}$ for $\Delta\lambda = 45°$). Here, error bars indicate the uncertainty arising from the re-binning process after picking 20 random seed locations, and it therefore only affect angular scales larger than 5°. Also, the I values obtained for $\Delta\lambda = 5°$ are extremely similar to the values retrieved for an ideal spheromak structure observed at the same angular scale (as discussed in Section 3.1). The maximum separation at which the Moran's I remains above 0.5 for all distances and seed locations considered is $\Delta\lambda = 25°$ (corresponding to $F_{\omega/2} = 0.55$ of the initial CME half angular width), as marked by the white dotted line in Figure 4 (a). This also indicates similar levels of clustering in the spatial arrangement of the ME class between the ME in run A and the ideal spheromak structure. From these results we conclude that spacecraft swarms composed of at least 7–12 evenly-spaced spacecraft crossing the same ME structure at different impact angles from the center to the flanks measure a highly-clustered distribution of ME types and generally a low level of ME magnetic complexity, while swarms that are more widely separated observe a high-complexity structure with a randomly-arranged ME type distribution.

The spatial autocorrelation of ME classes within an ME behaves differently when interactions with other structures affect its propagation. In run B (Figure 4 (b)), the ME initially has a similar complexity than in run A, as indicated by the Moran's I ranging between $0.94^{+0.00}_{-0.00}$ for $\Delta\lambda = 5°$ and $0.28^{+0.00}_{-0.27}$ for $\Delta\lambda = 45°$ at 0.3 au. Small separations also report higher Moran's I values than large separations: at this stage, we observe a low complexity ($I > 0.5$) up to $\Delta\lambda = 25°$ of separation (corresponding to $F_{\omega/2} = 0.55$ of the initial CME half angular width), and a high complexity at larger separations. However, in contrast with run A, the characteristic scale of transition from a low ($I > 0.5$) to a high ($I \leq 0.5$) complexity decreases with heliocentric distance, likely due to the interaction of the ICME with the HSS/SIR. Specifically, we observe a transition in the location of the $I = 0.5$ threshold from $\Delta\lambda = 25°$ (corresponding to $F_{\omega/2} = 0.55$ of the initial CME half angular width) to $\Delta\lambda = 20°$ of separation (corresponding to $F_{\omega/2} = 0.44$) near 0.6 au. By the time the ME reaches 1.6 au, the range covered by the Moran's I is between $0.90^{+0.00}_{-0.00}$ for $\Delta\lambda = 5°$ and $\sim 0.32^{+0.00}_{-0.38}$ for $\Delta\lambda = 45°$, i.e. similar to the values retrieved in run A, but we observe a clear decreasing trend with respect to the heliocentric distance at all scales $\lesssim 20°$, where the Moran's I values at 1.6 au are significantly smaller than the initial values retrieved at 0.3 au. This can be seen in the fact that the error bars inferred from the consideration of 20 random seed locations do not overlap. No clear trend with respect to the heliocentric distance is apparent at larger scales (where the values at 0.3 au and 1.6 au are consistent within the error bars inferred from the
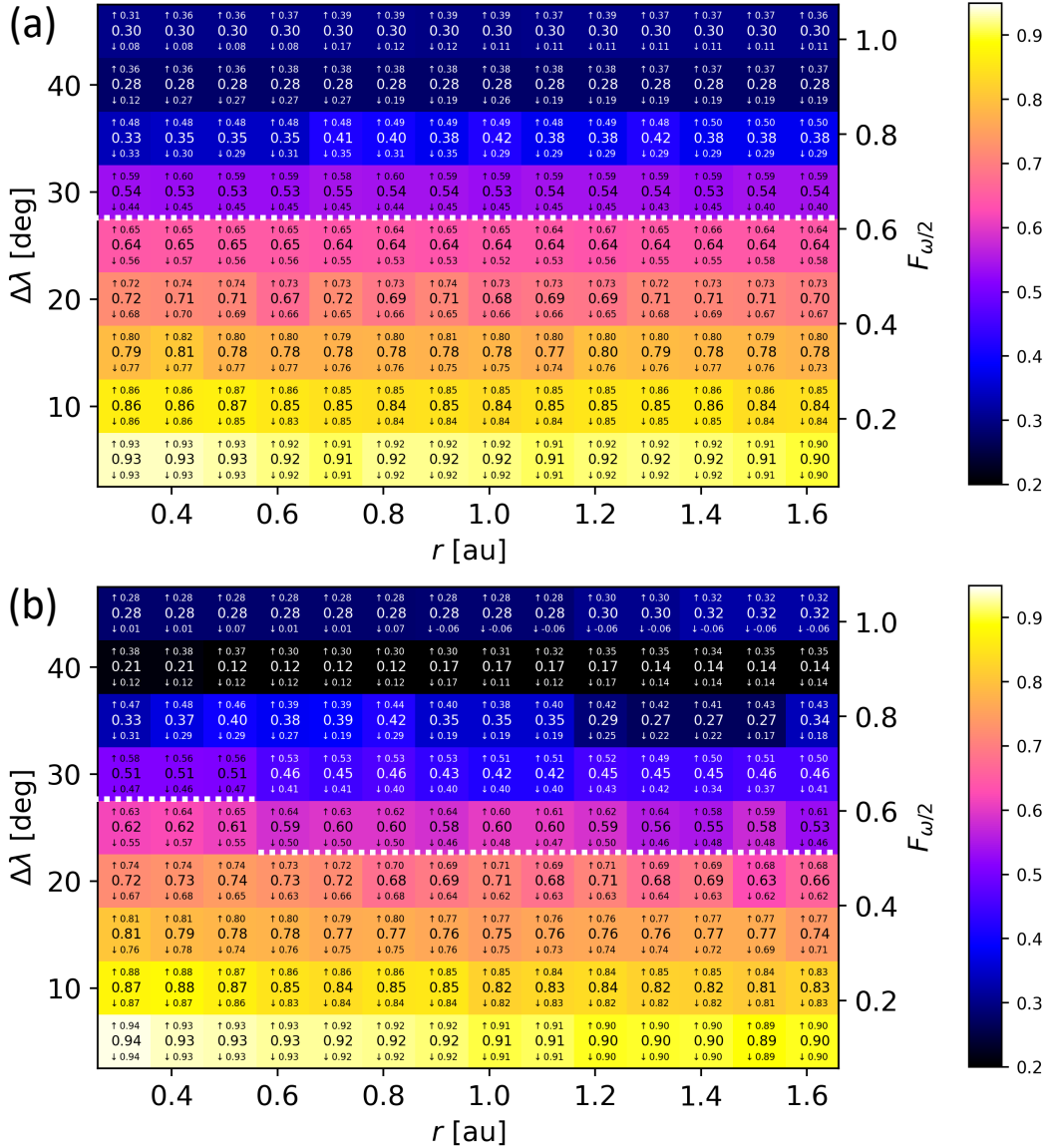
Figure 4. Moran's I as a function of the spacecraft separation $\Delta\lambda$ and heliocentric distance r, for the two ICMEs simulated in EUHFORIA. (a): Moran's I resulting from run A. (b): Moran's I resulting from run B. The color code and values overplotted in each cell indicate the Moran's I obtained for a seed location at $(\theta_s, \phi_s) = (0°, 0°)$, while the $\uparrow$ and $\downarrow$ symbols indicate the uncertainty (i.e. the spread, corresponding to the range of maximum and minimum values) as obtained by picking 20 random seed locations. The dotted white lines distinguish between regions where $I > 0.5$ (considered regions with well-ordered distribution of ME types and low magnetic complexity) and regions where $I \leq 0.5$ (considered regions with randomly-ordered distribution of ME types and high magnetic complexity).

consideration of 20 random seed locations), indicating at these scales no changes to the global ME magnetic complexity are detected during propagation. Overall, these results indicate that the magnetic complexity quantified in terms of the spatial autocorrelation of ME types observed across different directions is affected by the interaction with the HSS/SIR structure only at separation scales as large as $\Delta\lambda = 20°$ (at spatial scales $F_{\omega/2} \leq 0.44$ of the initial CME half angular width). This corresponds to having a minimum of 13–16 spacecraft crossings through the same ME to capture the evolutionary trends in the clustering of ME types, as swarms separated by larger separations would consistently observe a highly-randomized spatial distribution of ME types and complexity regardless of the specific ME propagation history.
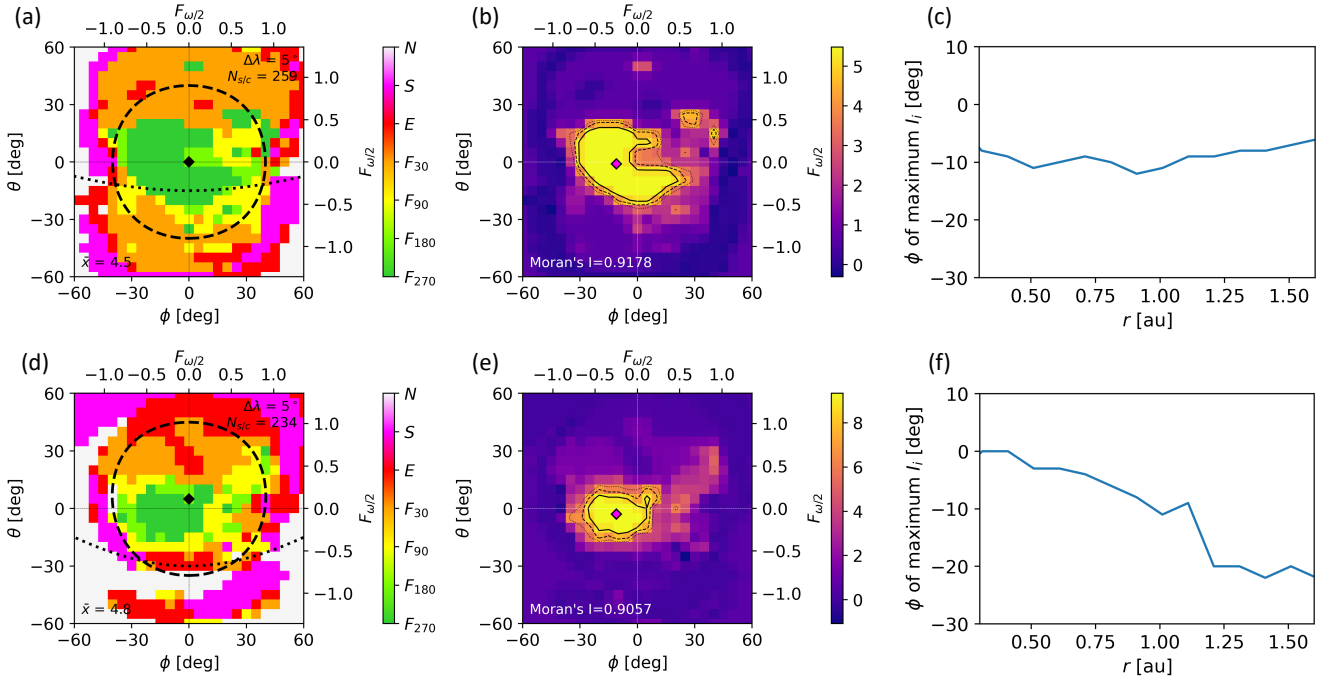
Figure 5. Analysis of the Local Moran's I near 1 au for the two ICMEs simulated in EUHFORIA. (a), (d): ME type distribution at 1 au (color coded), for run A and B, respectively. (b), (e): distribution of the Local Moran's I (I_i) at 1 au (color coded), for run A and B, respectively. The locations of the maximum of the Local Moran's I ($\max(I_i)$) are indicated by the magenta diamonds, while contours denote the $[0.9, 0.75, 0.6] \max(I_i)$ levels. (c), (f): longitude of the maximum of the Local Moran's I, as a function of the heliocentric distance.

To confirm the role of the interaction with the HSS/SIR as source of the Moran's I increase with heliocentric distance in run B, we consider the spatial distribution of the Local Moran's I as a function of the heliocentric distance in both EUHFORIA runs. Figures 5 (a) and (d) show the spatial distribution of ME types for runs A and B near 1 au which we use to derive the Local Moran's I distributions reported in Figures 5 (b) and (e). To determine the complexity increase affecting different ME regions, we track the (θ, ϕ) position of its maximum value (marking the lowest complexity region) as a function of the heliocentric distance. In run A we find that the $\phi_{\max(Ii)}$ remains between $-5°$ and $-10°$ at all heliocentric distances considered (Figure 5 (c)). The fact that the location of lowest complexity within the ME does not change with heliocentric distance is consistent with the lack of interactions altering the ME structure. In run B, on the other hand, we observe that the maximum Local Moran's I progressively drifts towards the east with respect to the Sun–Earth line, with $\phi_{\max(Ii)}$ shifting from $0°$ at 0.3 au to $-23°$ at 1.6 au (Figure 5 (f)). In other words, during its propagation the ME retains a low complexity only on the easternmost region, while the westernmost region progressively increases its complexity. This is consistent with the westernmost ME portion being more heavily affected by the interaction with the HSS/SIR, which may be the prime source of increased complexity in that region of the ME. Interestingly, we also note that even in run A, $\phi_{\max(Ii)}$ is slightly offset with respect to the Sun–Earth line. In the absence of any interplanetary structure in the simulated ambient solar wind that could have induced such a longitudinal asymmetry in the spatial distribution of ME complexity, we consider this result to be intrinsic to the propagation of the ICME through a Parker magnetic field spiral, which presents an intrinsic asymmetry with respect to the ICME propagation direction. Such an interpretation is further corroborated by the results obtained from the spatial analysis of magnetic coherence presented below in Section 3.4.

3.4. *Characteristic Scales of Magnetic Coherence during Propagation*

In this section, we investigate the scale at which an ME may be able to respond to external perturbations in a coherent manner. For this purpose, we consider the correlation of magnetic field components between different observers as a proxy for the scale of magnetic coherence, similarly to previous observational investigations (Wicks et al. 2010; Lugaz et al. 2018; Ala-Lahti et al. 2020). Determining across which spatial scales MEs exhibit coherent characteristics is a
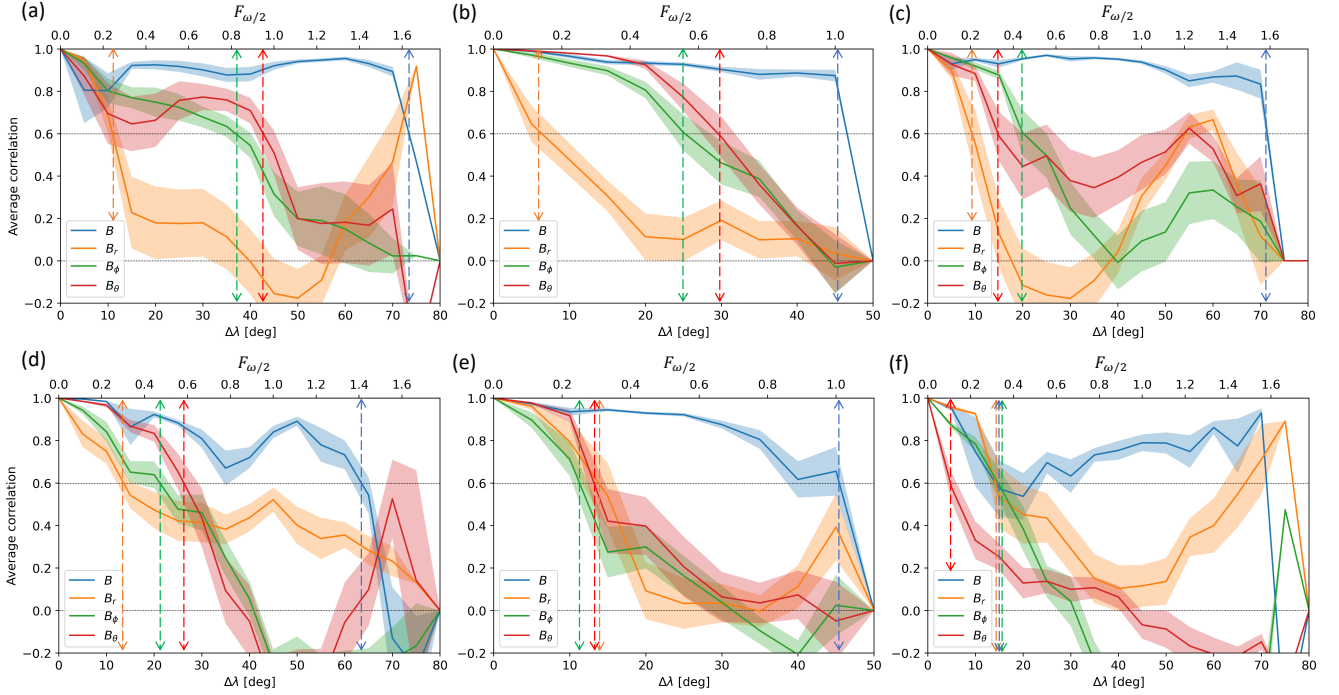
Figure 6. Average correlation profiles for the magnetic field magnitude and components at 1 au, for run A (top) and run B (bottom) in EUHFORIA. Three reference observers are considered: one on the east (left), one near the center (center), and one on the west (right) of the ME. In all panels, the solid lines indicate the correlations calculated by averaging across all possible directions with respect to the reference observer, while the shaded areas represent the error bars estimated from the standard errors, i.e. $\pm\mathrm{SE}_{\mathrm{corr}B}$, $\pm\mathrm{SE}_{\mathrm{corr}Br}$, $\pm\mathrm{SE}_{\mathrm{corr}B\theta}$, $\pm\mathrm{SE}_{\mathrm{corr}B\phi}$, obtained from considering different directions around the reference observer. The average radii of correlation, measures of the characteristic correlation scales within the ME, are marked by the dashed arrows.

first, necessary step towards a better understanding the global response of ME structures to external perturbations induced by the surrounding environment. As reference directions to investigate the scales of magnetic coherence, we consider hypothetical observers crossing the ME structures in regions differently affected by the interaction of the ICME with the surrounding wind and, in run B, with the large-scale structures therein. Such reference directions are located along the equatorial plane of the ME ($\theta_{\mathrm{ref}} = \theta_{\mathrm{CME}}$) and at ϕ_{ref} angles of $-30°$, $0°$, and $30°$, i.e. corresponding to observers crossing the ME magnetic structure on the east, center, and west regions near its central magnetic field axis. Figure 6 shows the results of the analysis for the average correlation scale of the magnetic field magnitude and the B_r, B_θ and B_ϕ components for run A (panels (a) to (c)) and B (panels (d) to (f)) at 1 au, for these three reference observers.

By comparing the results from runs A (Figure 6 (a)–(c)) and B (Figure 6 (d)–(f)), we find that all magnetic field components (except for B_r) have smaller average correlation scales in run B than in run A, indicating interactions may significantly reduce the ability of MEs to behave as magnetically coherent structures. For an observer crossing near the center of the ME, B remains highly correlated throughout the whole magnetic structure ($\Delta\lambda = 45°$, corresponding to $F_{\omega/2} = 1.00$ of the initial CME half angular width) for both runs A (panel (b)) and B (panel (e)). These scales are slightly higher than those reported for an ideal spheromak structure ($\Delta\lambda = 40°$, $F_{\omega/2} = 0.88$, not shown). We speculate that expansion/deformation mechanisms (such as those reported within 0.3 au by Scolini et al. (2021a); see Figure 12 therein) may be acting across the whole ME cross-section during early propagation phases (from 0.1 to 0.3 au) leveling out spatial asymmetries in the total magnetic field profile. The average correlation scales for B_θ and B_ϕ drop from $\Delta\lambda \sim 25° - 30°$ ($F_{\omega/2} \sim 0.55 - 0.66$) in run A, to $\Delta\lambda \sim 10° - 15°$ ($F_{\omega/2} \sim 0.22 - 0.33$) in run B. In run A the correlation scale is already significantly reduced compared to the ideal spheromak case (where $\Delta\lambda = 40°$, $F_{\omega/2} = 0.88$, not shown), and even more so in run B. Only the average correlation scale for B_r slightly increases from $\Delta\lambda = 5°$ ($F_{\omega/2} = 0.11$) to $\Delta\lambda = 15°$ ($F_{\omega/2} = 0.33$), and both runs report higher correlation scales than in the ideal spheromak case (where the correlation was lost only a few degrees away from the reference observer). However,

$SE_{corr Br}$ is generally larger than for the other components in both EUHFORIA runs, reflecting the fact that the actual average correlation scale is highly asymmetric around the reference observer, and therefore is affected by large error bars.

The results are qualitatively the same for an observer crossing through the east and west of the ME. For both observers, B remains highly correlated throughout the whole magnetic structure in both runs A and B ($\Delta\lambda = 65° - 70°$, corresponding to $F_{\omega/2} = 1.44 - 1.55$). The average correlation scales for B_θ and B_ϕ reduce by a factor ~ 2 or more between run A and run B. For an east observer, the correlations reduce from $\Delta\lambda \sim 35° - 45°$ ($F_{\omega/2} \sim 0.77 - 1.00$) in run A to $\Delta\lambda \sim 20° - 25°$ ($F_{\omega/2} \sim 0.44 - 0.55$) in run B. For a west observer, the average correlation scale for B_θ decreases from $\Delta\lambda = 15°$ ($F_{\omega/2} = 0.33$) to $\Delta\lambda = 5°$ ($F_{\omega/2} = 0.11$), while that of B_ϕ decreases from $\Delta\lambda = 20°$ ($F_{\omega/2} = 0.44$) to $\Delta\lambda = 15°$ ($F_{\omega/2} = 0.33$) between run A and B. These results clearly demonstrate how correlations for a west observer in B_θ and B_ϕ are up to a factor 4 smaller than correlations for an east observer. The average correlation scale for B_r remains roughly constant around $\Delta\lambda \sim 10° - 15°$ ($F_{\omega/2} \sim 0.22 - 0.33$) in both runs.

It is worth mentioning that even in the case without interactions, smaller correlation scales are found for a west observer compared to an east observer. Due to the lack of structures in the simulated ambient solar wind in run A, we consider this result to be linked to the propagation of the ICME through a magnetic field characterized by a Parker spiral configuration, which presents an intrinsic asymmetry with respect to the ICME propagation direction that leads to different ICME–solar wind interaction behaviors at the two ICME flanks (e.g. in terms of pressure balance; see Wang et al. 2004). Differences between the east and west observers are even more pronounced in run B, and this is interpreted as due to the superposition of the effects related to the east-west Parker spiral asymmetry, and the interaction with the HSS/SIR mainly affecting the western portion of the ICME.

In light of these results, we clarify why we use a different definition of correlation scale compared to observational works (Lugaz et al. 2018; Wicks et al. 2010). First of all, in both the ideal spheromak structure and EUHFORIA simulations we found no scale at which correlations in the B, B_θ and B_ϕ components reach values near zero. This is more likely due to the very idealized ME structure considered, while actual MEs may have more complex configurations already following their eruption in the low solar corona and before reaching 0.1 au. Secondly, contrary to the ME and solar wind profiles reported by Lugaz et al. (2018) and Wicks et al. (2010), our correlation does not scale in a quasi-linear or quasi-exponential manner, so we decided to refrain from fitting curves with specific functions and rather defined a measure of coherence that was more appropriate for our specific problem.

Despite these methodological differences, the results retrieved in our numerical simulations have several elements in common with observational estimates. Specifically, the ranking of the average correlation scales for the different magnetic field components (with B and B_r being the most and least correlated, respectively) is consistent with what was found within an ideal spheromak structure and with estimates obtained from in situ observations of real MEs by Lugaz et al. (2018). Furthermore, the range of average correlation scales for B (estimated around $45°$ for a central observer, and $15°$ to $70°$ for a flank observer) encompasses previous constraints on the characteristic scale of magnetic coherence at 1 au by Lugaz et al. (2018) ($12° - 20°$) and Owens (2020) ($\sim 26°$). The range of average correlation scales for B_θ and B_ϕ (estimated around $10°$ to $30°$ for a central observer, and between $5°$ and $45°$ for a flank observer) also encompasses previous estimates on the characteristic scale of magnetic coherence at 1 au for the magnetic field components, reported in range $4° - 7°$ by Lugaz et al. (2018). The larger upper limit found in our study is somewhat expected: the global, ideal MHD nature of our numerical model, as well as the simplified set-up used in this study (including the insertion of a perfectly-known global CME magnetic structure at the inner boundary of the heliospheric domain, located at 0.1 au in our simulations) likely resulted in a more regular/smooth magnetic configuration in simulated MEs compared to real MEs at the same heliocentric distance. Additionally, we note the diverse nature of previous studies (in terms, e.g., of working assumptions, data sets, range of parameters explored) when compared to each other and to this investigation, which may have also led to different coherence scale estimates across these studies.

We conclude the analysis of magnetic coherence by considering the evolution of the ME average correlation scales with heliocentric distance. In Figure 7, we show the ME average correlation scales for the total magnetic field and the three magnetic field components, as a function of the heliocentric distance, for the two EUHFORIA simulations and a reference observer crossing near the ME center. We find that the characteristic correlation scales for an ICME propagating through a homogeneous solar wind are unchanged during its propagation (Figure 7 (a)), remaining around $F_{\omega/2} = 1$ for B, $F_{\omega/2} = 0.44 - 0.66$ for B_θ and B_ϕ, and below $F_{\omega/2} = 0.22$ for B_r at all heliocentric distances. On the other hand, an interaction with a HSS/SIR induces a clear decrease in the ME average correlation scales during propagation, particularly for B_θ and B_ϕ (Figure 7 (b)). The decrease is more rapid between 0.3 au and 1 au, while it
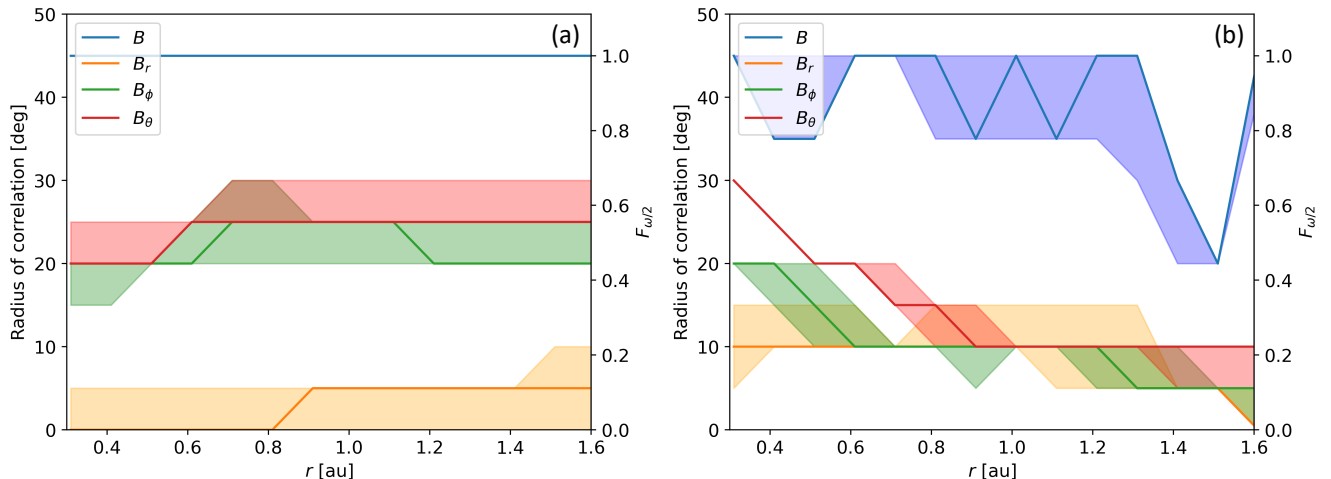
Figure 7. Characteristic scale of correlation for the total magnetic field and the three magnetic field components, as a function of the heliocentric distance, for the two spheromak CMEs simulated in EUHFORIA. The reference location is taken at $(\theta, \phi) = (0°, 0°)$ for run A (a), and $(\theta, \phi) = (5°, 0°)$ for run B (b), corresponding to the CME initial direction in the two simulations. In all panels, the continuous lines indicate the average correlation scale with respect to the reference observer, while the shaded areas represent the error bars on the average correlation scale estimated from the standard errors, i.e. $\pm\mathrm{SE}_{\mathrm{corr}B}$, $\pm\mathrm{SE}_{\mathrm{corr}Br}$, $\pm\mathrm{SE}_{\mathrm{corr}B\theta}$, $\pm\mathrm{SE}_{\mathrm{corr}B\phi}$, obtained from considering different directions around the reference observer.

continues at smaller rates up to 1.6 au. Overall, the maximum scale of correlation reduces from $F_{\omega/2} = 1$ to 0.44 for B, from $F_{\omega/2} = 0.66$ to 0.11 for B_θ, from $F_{\omega/2} = 0.44$ to 0 for B_ϕ, and from $F_{\omega/2} = 0.33$ to 0 for B_r between 0.3 au and 1.6 au. Interactions with other large-scale structures may therefore induce a decrease by a factor of 3 to 6 in the ME magnetic field correlation scales.

4. IMPLICATIONS FOR ECLIPTIC MISSIONS

In this section, we focus on spacecraft near the CME equatorial plane (which is close to the solar equatorial and ecliptic planes in our particular case) in order to support the planning and interpretation of observations by future multi-spacecraft missions exploring ICME structures in the ecliptic plane. The simulation set-up considered here specifically applies to spacecraft in the near-ecliptic region that cross through low-inclination FRs, which constitute about half of the ME FR configurations detected within 1 au (e.g. Lepping et al. 1990; Bothmer & Schwenn 1998; Lynch et al. 2003), and the majority of cases observed between 1 au and 2.2 au (Davies et al. 2022).

In order to determine the main implications for ecliptic missions, we focus on spacecraft crossings in our EUHFORIA-simulated ICMEs close to the ecliptic plane and near the spheromak central magnetic axis, i.e. at $\theta = \theta_{\mathrm{CME}}$. θ_{CME} corresponds to $\theta = 0°$ in run A and to $\theta = 5°$ in run B, and we chose these latitudinal values to more fairly compare crossings across the ICMEs between the two runs. The main results are displayed in Figure 8 (a) and (b), which show the spatial distribution of ME types detected at different heliocentric distances by simulated spacecraft located at $\theta = \theta_{\mathrm{CME}}$ in runs A and B. In the case of run A, i.e. ICME with no interaction, Figure 8 (a) shows a relatively well-ordered distribution of ME types, with spacecraft aligned in different radial directions recording similar ME types as the ME propagates to larger heliocentric distances. The dominance of F_{270} and F_{180} types (associated with $\mathbb{C} = 0$ and 1, respectively) suggests the ME is less complex in its equatorial region than it is globally. This result is consistent with the spatial distribution of ME types obtained for an ideal spheromak structure (as shown in Figure 6 (d) in Scolini et al. (2021b)). Interestingly, we find that even without interactions with large-scale structures, a change in the most frequently observed ME type is observed around 0.8 au, where F_{270} types are taken over by F_{180}. F_{270} types are initially dominant and spread across different directions, but progressively concentrate only in the eastern part of the ME, while F_{180} types become dominant in the western part. As discussed above, this is likely a reflection of Parker spiral effects induced by propagation through an asymmetric interplanetary magnetic field. F_{90}, F_{30}, and E types (corresponding to $\mathbb{C} = 2, 3$ and 4, respectively) are all very rarely observed in the ecliptic plane, making up less than 20% of the observed cases. The analysis of the results considering different angular separations (not shown) reveals that only spacecraft separated by $\Delta\lambda \lesssim 15°$ ($F_{\omega/2} \lesssim 0.33$, corresponding to ~ 6 spacecraft crossing the ME in different
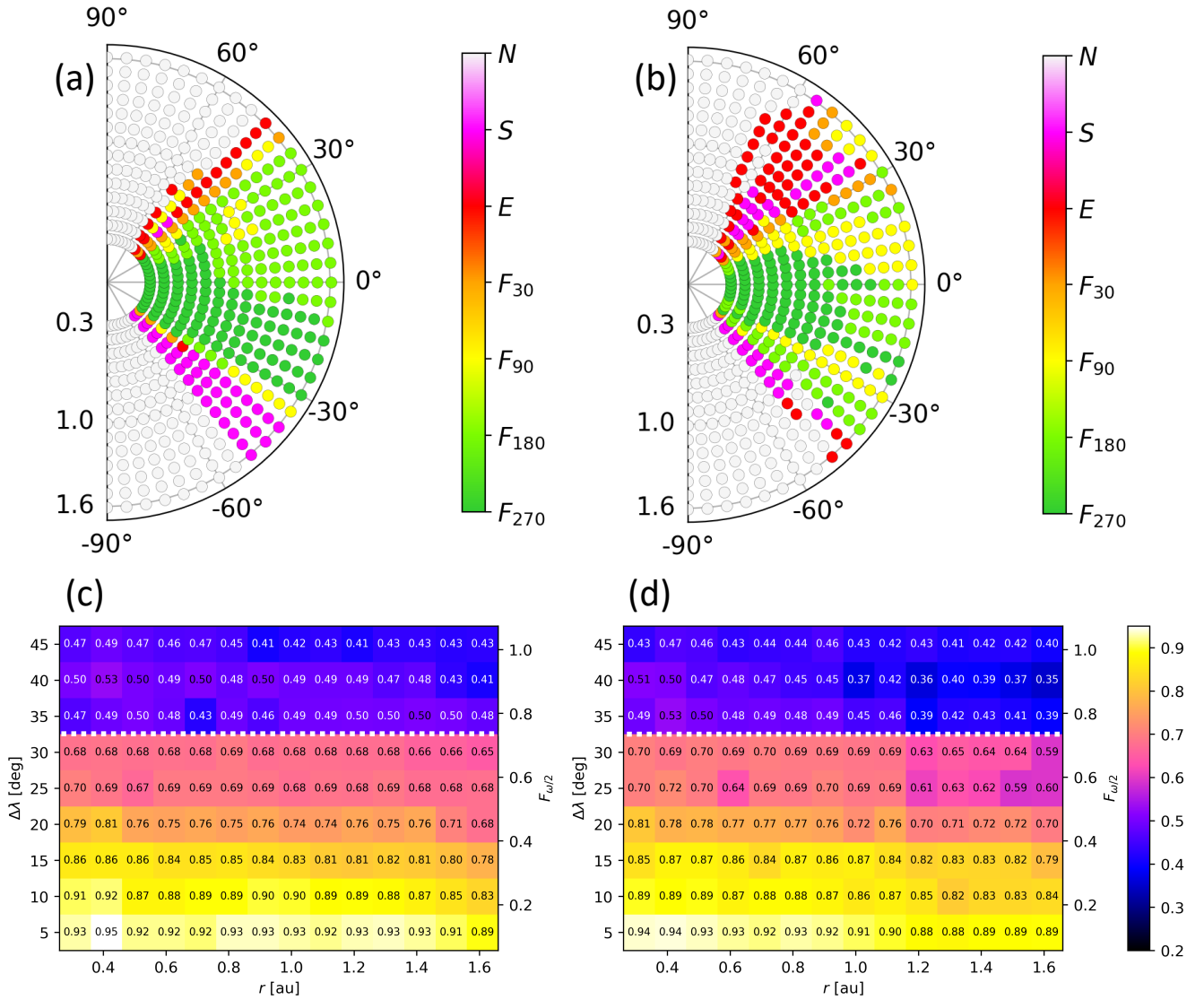
Figure 8. Analysis of the ME type distribution and Moran's I as a function of the heliocentric distance, at $\theta = \theta_{\mathrm{CME}}$, for the two ICMEs simulated in EUHFORIA. (a), (b): distribution of ME types (color coded) as a function of the heliocentric distance and longitude for runs A and B, respectively. (c), (d): Moran's I (also color coded) as a function of the heliocentric distance and spacecraft separation $\Delta\lambda$, for runs A and B, respectively. The dotted white lines distinguish between regions where $I > 0.5$ (considered regions with well-ordered distribution of ME types and low magnetic complexity) and regions where $I \leq 0.5$ (considered regions with randomly-ordered distribution of ME types and high magnetic complexity).

directions near its central axis) can characterize the ecliptic complexity of the ME observed by spacecraft at $\Delta\lambda \lesssim 5°$ ($F_{\omega/2} \lesssim 0.11$) across all heliocentric distances. However, we emphasize that regardless of their angular separation, observations in the ecliptic plane alone are not sufficient to characterize the global complexity of the ME (where F_{270} and F_{30} were the two dominant ME types; see Section 3.2), and off-ecliptic observations are therefore required.

In run B (ICME with interaction), we observe a much more irregular distribution of the ME types in both the longitudinal and radial directions (Figure 8 (b)). On the ME equatorial plane we find that the most common ME types are F_{270} up until 1 au, after which F_{180}, F_{90} and E types become comparable. Just as for run A, we therefore conclude that the ME is less complex near its central axis than it is globally. Results at different angular separations also indicate that a swarm of at least $\gtrsim 9$ near-equatorial spacecraft separated by $\Delta\lambda \lesssim 10°$ ($F_{\omega/2} \lesssim 0.22$) would be required to capture the ecliptic ME spatial complexity and its evolution across all heliocentric distances. Furthermore,

similarly to the case of run A, off-ecliptic observations are required to characterize the global complexity of the ME as discussed in Section 3.2.

To calculate the Moran's I, we have to consider a 2-D spacecraft array distributed in longitude and latitude (see Equation 1). Therefore, we compute the Moran's I at each heliocentric distance from near-equatorial regions in EUHFORIA simulations by considering a near-equatorial array of spacecraft within $\pm 15°$ from $\theta = \theta_{CME}$. This array consists of $\Delta\phi = \Delta\theta = 5°$ separated spacecraft arranged in $3 \times 2 + 1 = 7$ latitudinal rows. Figure 8 (c) and (d) report the results of the analysis. In general, we observe higher values of $I(r)$ compared to Figure 4, indicating that the ME exhibits a higher spatial autocorrelation in near-equatorial regions than it does in the perpendicular direction. We obtain a similar result in the case of an ideal spheromak structure (not shown), suggesting that an ideal or weakly-perturbed spheromak structure is particularly ordered near its magnetic axis. For run A (Figure 8 (c)), we find that at all heliocentric distances, $I(r)$ decreases with $\Delta\lambda$ and remains above 0.5 up until $\Delta\lambda = 30°$ ($F_{\omega/2} = 0.66$), which is slightly larger than the separation scale obtained when considering the whole ME structure (Figure 4 (a)). This further confirms the higher spatial clustering of ME types within the ME in the near-equatorial regions compared to other directions. Results are also slightly decreasing with heliocentric distance at scales $\Delta\lambda \leq 20°$ ($F_{\omega/2} = 0.44$), while they are independent on the propagation phase at larger angular separations. For run B (Figure 8 (d)), we obtain similar results to run A in terms of the scale at which $I(r)$ becomes smaller than 0.5 ($\Delta\lambda = 30°$, corresponding to $F_{\omega/2} = 0.66$). However, we also notice that $I(r)$ shows a more clear dependence on the heliocentric distance up to scales $\Delta\lambda \leq 40°$ ($F_{\omega/2} = 0.88$), suggesting that the perturbation to the ME induced by the interaction with the HSS/SIR extends across a wider range of angular scales in the near-equatorial plane compared to other directions (Figure 4 (b)).

The correlation with respect to a central reference observer tends to be maximum along the ME magnetic axis (i.e. near the equatorial plane): focusing on the results at $\theta = \theta_{CME}$, we find that for both an ideal spheromak structure (not shown) and for run A (as shown in Figure 9 (a) to (d)), the correlation extends throughout the whole ME width. These results confirm that an ideal or weakly-perturbed spheromak structure exhibits coherent signatures across wider scales particularly along its principal magnetic axis. In run B (panels (e) to (h)), the correlation scale remains generally large for B up to 1.3 au, and it then reaches a minimum of $5°$ ($F_{\omega/2} = 0.11$) in the west direction and $20°$ ($F_{\omega/2} = 0.44$) in the east direction around 1.5 au. For B_θ and B_ϕ, the ME westernmost region becomes progressively more perturbed than the easternmost one during propagation, up to the point of losing all correlations with a central reference observer. Near 1.5 au, the correlation scale is between $\lesssim 5°$ ($F_{\omega/2} \lesssim 0.11$) in the west direction and $35°$ ($F_{\omega/2} = 0.77$) in the east direction for B_ϕ; and between $5°$ ($F_{\omega/2} = 0.11$) in the west direction and $45°$ ($F_{\omega/2} = 1$) in the east direction for B_θ.

Finally, we note that for spacecraft crossings near the spheromak magnetic field axis (either for an ideal spheromak structure, or in EUHFORIA simulations), ME signatures are expected to be similar to the ones encountered by crossing near the axis of cylindrical FR geometries, i.e. with bipolar B_θ signatures and nearly-unipolar signatures in B_ϕ (see Figure 6 in Scolini et al. 2021b). Results along the direction $\theta = \theta_{CME}$ in each EUHFORIA simulation can therefore be expected to be less dependent on the specific FR model used than in other directions, and we hypothesize they could be potentially extrapolated to other FR models as well. For the opposite reason, the most severe difference between the spheromak model and other cylindrical FR models is expected to be found in the direction perpendicular to the magnetic axis (e.g. as in the case of ecliptic crossings through high-inclination FR types), but we leave the consideration of this alternative scenario for future studies.

5. CONCLUSIONS

In this study, we presented an in-depth investigation of the spatial scales of magnetic complexity and coherence within MEs as inferred from spacecraft swarms in global heliospheric simulations based on the consideration of various ICME-solar wind interaction scenarios and different complexity and coherence metrics. This work is also the first-ever attempt to investigate ME magnetic coherence scales by analyzing the results of global numerical simulations in an observationally-consistent fashion. Specifically, we evaluated the magnetic complexity of the simulated MEs based on the frequency of ME types detected by virtual spacecraft crossing the MEs along different directions during their propagation through interplanetary space. We further explored the spatial distribution of magnetic complexity within the simulated MEs using the Moran's I spatial autocorrelation index. We determined the characteristic scale of magnetic coherence within the MEs by evaluating the maximum angular separation at which virtual spacecraft crossing the same ME observed magnetic field signatures highly correlated to those detected by a reference observer.
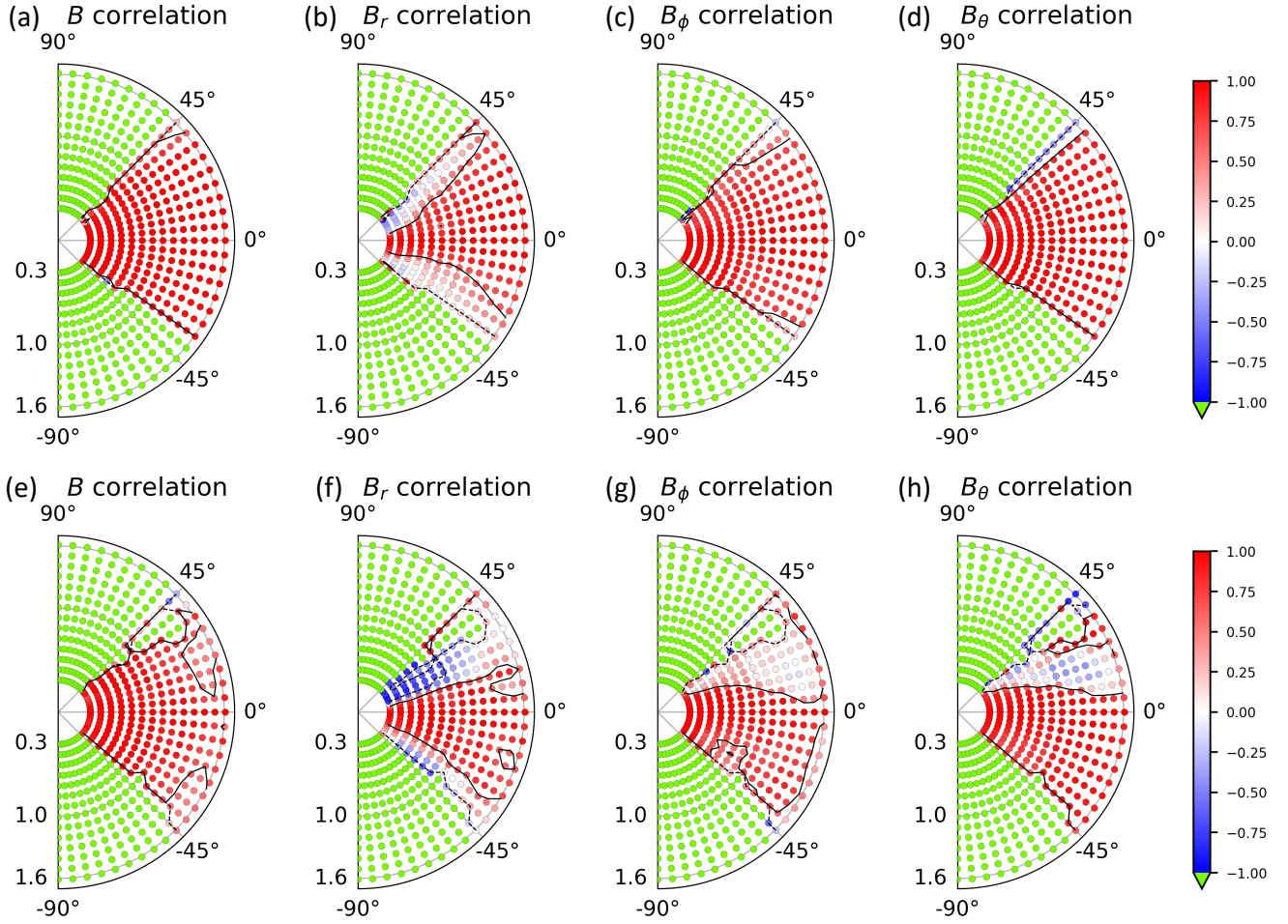
Figure 9. Correlation maps (color coded) for the total magnetic field and the three magnetic field components with respect to a central reference observer ($\phi_{\rm ref} = 0°$), as a function of the heliocentric distance and longitude at $\theta = \theta_{\rm CME}$, for run A (top) and run B (bottom) in EUHFORIA. (a), (e): B. (b), (f): B_r. (c), (g): B_ϕ. (d), (h): B_θ. In each panel, black contours mark regions were the correlation is $+0.6$ (continuous lines) or -0.6 (dashed lines).

	Whole structure		Equatorial plane	
	Run A	Run B	Run A	Run B
Complexity: ME types	$25°(0.55)$	$10°(0.22)$	$15°(0.33)$	$10°(0.22)$
Complexity: autocorrelation	$25°(0.55)$	$20°(0.44)$	$30°(0.66)$	$30°(0.66)$
Coherence: B	$45°(1.00)$	$20–45°(0.44–1.00)$	$35–40°(0.77–0.88)$	$5–20°(0.11–0.44)$
Coherence: B_r	$0–10°(0.00–0.22)$	$0–5°(0.00–0.11)$	$10–25°(0.22–0.55)$	$5–10°(0.11–0.22)$
Coherence: B_θ	$15–30°(0.33–0.66)$	$0–5°(0.00–0.11)$	$35–40°(0.77–0.88)$	$5–45°(0.11–1.00)$
Coherence: B_ϕ	$20–30°(0.44–0.66)$	$5–10°(0.11–0.22)$	$30–35°(0.66–0.77)$	$5–35°(0.11–0.77)$

Table 1. Summary of the characteristic scales of complexity and coherence within MEs for a central observer (between 0.3 and 1.6 au) retrieved in this work. Values are expressed in terms of the spacecraft angular separation $\Delta\lambda$ and of the fraction of CME initial half angular width $F_{\omega/2}$ (in brackets).

A summary of the characteristic scales derived from numerical simulation between 0.3 and 1.6 au is provided in Table 1, and the main conclusions are summarized as follows:

1. On the one hand, analyses of the frequency and spatial clustering of ME types within MEs indicate that their global magnetic complexity does not change with heliocentric distance if no interaction with other large-scale

solar wind structures occurs during their propagation. On the other hand, the ME magnetic complexity is likely to increase during its propagation if interactions with other large-scale solar wind structures occur, confirming previous results by Winslow et al. (2016, 2021b) and Scolini et al. (2021b, 2022).

2. The two global magnetic complexity metrics considered (frequency of ME types, and the Moran's I spatial autocorrelation index) both indicate that the consideration of smaller angular scales is required to capture global complexity changes in the presence of interactions. As demonstrated in Section 3.2, for an ICME with initial half angular width of $45°$ as the one simulated in this work, the spatial characterization of the occurrence of ME types requires in situ observations at separations no larger than $\Delta\lambda = 25°$, but separations no larger than $\Delta\lambda = 10°$ are needed in the case of ICME–solar wind interacting scenarios. Section 3.3 proved that the analysis of the spatial autocorrelation of ME types via the Moran's I coefficient requires observations at separations up to $\Delta\lambda = 25°$ for a non-interacting ICME, which reduces to $\Delta\lambda = 20°$ or less for ICME–HSS/SIR interacting scenarios. The angular separations above are more conveniently expressed in terms of scale-invariant quantities, particularly as fractions of the CME initial half angular width ($F_{\omega/2}$) and in terms of the associated number of virtual spacecraft required to cross the ME structure, which are independent of the prescribed initial CME half angular width and can therefore be extrapolated to CMEs of different sizes. In this respect, we found that the spatial characterization of the occurrence of ME types within an ME requires in situ observations at separations $F_{\omega/2} \leq 0.55$, corresponding to a minimum of 7 to 12 spacecraft crossings. Separations $F_{\omega/2} \leq 0.22$, corresponding to a minimum of 50 to 65 spacecraft crossings, are needed in the case of ICME–solar wind interacting scenarios. The analysis of the spatial autocorrelation of ME types via the Moran's I coefficient requires observations at separations up to $F_{\omega/2} = 0.55$, corresponding to 7 to 12 spacecraft crossings for a non-interacting ICME, which reduces to $F_{\omega/2} \leq 0.44$, corresponding to 13 to 16 spacecraft crossings or less for ICME–HSS/SIR interacting scenarios.

3. In our numerical simulations, the scale of correlation of the magnetic field components within MEs was different for different components, and tended to be the largest for B, followed by B_θ and B_ϕ, and ultimately by B_r. As discussed in Section 3.4, the characteristic scale of correlation reduced by a factor of 3–6 for MEs within ICMEs interacting with preceding HSSs/SIRs ($\Delta\lambda = 5°$, corresponding to $F_{\omega/2} = 0.11$) compared to ICMEs that do not interact with other large-scale structures ($\Delta\lambda = 15° - 30°$, corresponding to $F_{\omega/2} = 0.33 - 0.66$). Results at different heliocentric distances also indicated that as ICMEs propagate to larger heliocentric distances, intervening interactions may efficiently destroy any pre-existing correlation scale within their MEs. Overall, such results suggest that the scale of magnetic coherence of ME structures would be optimally investigated by having spacecraft crossing through them at angular separations between $\Delta\lambda = 15°$ and $30°$ ($F_{\omega/2} = 0.33 - 0.66$) in cases where no significant interactions with other large-scale interplanetary structures occur. However, angular separations down to $\Delta\lambda = 5°$ ($F_{\omega/2} = 0.11$) and below, are needed in cases where significant interactions with other large-scale interplanetary structures do occur.

   Similar conclusions were reached by Farrugia et al. (2011) when analyzing an ICME interacting with a following HSS/SIR and observed at 1 au by three spacecraft at $\sim 20°$ separation. At the time, the authors emphasized the need for numerical simulations and/or more in situ observations for a complete elucidation of ICMEs interacting with SIRs, and the present work helps identify the most appropriate scales to be targeted in future studies to fill in current observation and knowledge gaps. Additionally, our results indicate that achieving small spacecraft angular separations would be particularly important at larger distances from the Sun, as the correlation scale is found to progressively shrink during propagation, the longer the interaction with large-scale solar wind structures occurs. For the opposite reason, when considering multi-spacecraft observations obtained in radial alignment, making sure that the angular offset among the different spacecraft involved is smaller than the aforementioned expected scales of coherence would be most appropriate to distinguish changes in magnetic signatures that are actually due to evolutionary effects, rather than to the intrinsic lack of correlation affecting observations acquired at larger angular separation scales.

4. At least for fast ICMEs as the ones simulated in this work, the magnetic complexity inferred from the spatial autocorrelation of ME types via the Local Moran's I coefficient was found to be higher in the western portion of MEs than on the eastern one regardless of the presence or absence of interactions with other large-scale solar wind structures. Additionally, smaller correlation scales were found around a reference observer crossing on the

western portion of the ME, compared to one on crossing the eastern portion. East-west differences were more prominent when an interaction with a preceding HSS/SIR was involved, but were present also in the ICME propagating through a quasi-homogeneous solar wind. These results are found to be due to a combination of two effects: a Parker spiral contribution that affects both interacting and non-interacting ICMEs; and a contribution from the actual interaction of ICMEs with preceding large-scale solar wind structures, which is localized in the region most influenced by the interaction.

5. Analyses of the magnetic complexity and coherence in the near-ecliptic plane (approximately corresponding to the direction of the ME magnetic axis) in Section 4 indicated that MEs may exhibit a lower complexity, higher spatial autocorrelation, and higher coherence along their magnetic axis compared to perpendicular directions. In this case, a minimum of ~ 6 spacecraft crossings separated by $F_{\omega/2} \lesssim 0.33$ (corresponding to $\Delta\lambda \lesssim 15°$) is necessary to characterize the evolution of ME magnetic complexity in the near-equatorial plane, which increases to ~ 9 spacecraft ($\Delta\lambda \lesssim 10°$, corresponding to $F_{\omega/2} \lesssim 0.22$) when interaction with preceding HSSs/SIRs are involved. However, also in the case of interactions with preceding large-scale solar wind structures, near-ecliptic observations alone were not able to characterize the ME global, off-ecliptic complexity.

Overall, our estimates for the scale of magnetic correlation of B_θ and B_ϕ encompass previous constraints on the characteristic scale of magnetic coherence at 1 au, reported in range $4° - 7°$ by Lugaz et al. (2018). The range of correlation scales obtained for B is also consistent with previous estimates by Lugaz et al. (2018) ($12° - 20°$) and Owens (2020) ($\sim 26°$). However, due to the numerical model and set-up's specificities, and the multi-scale nature of the magnetic coherence problem, larger upper limits found in our study are somewhat expected. Additionally, while from an observational standpoint the correlation of magnetic field profiles among different locations within an ME has been regarded as a proxy for magnetic coherence (Lugaz et al. 2018), it also remains unclear how the ability of information to propagate across an ME affects its local properties, and how this relates to the ability of the same ME to use such information in order to resist deformation by external factors and behave as a coherent structure (Owens 2020). While this work helps constrain some of the critical scales controlling the evolution of ME structures, and establishes new pathways for the investigation of ME magnetic coherence by analyzing the results of global numerical simulations in an observationally-consistent fashion (i.e. using spacecraft swarms), in the future, we envisage more sophisticated numerical tools in combination with new data from recently-launched missions (e.g. Parker Solar Probe and Solar Orbiter) will help pinpoint the scale and meaning of magnetic coherence within ICMEs more precisely.

REFERENCES

Al-Haddad, N., Nieves-Chinchilla, T., Savani, N. P., Lugaz, N., & Roussev, I. I. 2018, SoPh, 293, 73, doi: 10.1007/s11207-018-1288-3

Al-Haddad, N., Nieves-Chinchilla, T., Savani, N. P., et al. 2013, SoPh, 284, 129, doi: 10.1007/s11207-013-0244-5

Ala-Lahti, M., Ruohotie, J., Good, S., Kilpua, E. K. J., & Lugaz, N. 2020, Journal of Geophysical Research (Space Physics), 125, e28002, doi: 10.1029/2020JA028002

Anselin, L. 1995, Geographical Analysis, 27, 93, doi: 10.1111/j.1538-4632.1995.tb00338.x

Bothmer, V., & Schwenn, R. 1998, Annales Geophysicae, 16, 1, doi: 10.1007/s00585-997-0001-x

Burlaga, L., Sittler, E., Mariani, F., & Schwenn, R. 1981, J. Geophys. Res., 86, 6673, doi: 10.1029/JA086iA08p06673

Burlaga, L. F. 1988, J. Geophys. Res., 93, 7217, doi: 10.1029/JA093iA07p07217

Cane, H. V., & Richardson, I. G. 2003, Journal of Geophysical Research (Space Physics), 108, 1156, doi: 10.1029/2002JA009817

Cranmer, S. R., Gibson, S. E., & Riley, P. 2017, SSRv, 212, 1345, doi: 10.1007/s11214-017-0416-y

Davies, E. E., Winslow, R. M., Scolini, C., et al. 2022, ApJ (under review)

Farrugia, C. J., Matsui, H., Kucharek, H., et al. 2005, Journal of Geophysical Research (Space Physics), 110, A09S13, doi: 10.1029/2004JA010968

Farrugia, C. J., Berdichevsky, D. B., Möstl, C., et al. 2011, Journal of Atmospheric and Solar-Terrestrial Physics, 73, 1254, doi: 10.1016/j.jastp.2010.09.011

Good, S. W., & Forsyth, R. J. 2016, SoPh, 291, 239, doi: 10.1007/s11207-015-0828-3

Gosling, J. T., Bame, S. J., McComas, D. J., & Phillips, J. L. 1990, Geophys. Res. Lett., 17, 901, doi: 10.1029/GL017i007p00901

Hidalgo, M. A. 2013, ApJ, 766, 125, doi: 10.1088/0004-637X/766/2/125

Hidalgo, M. A., & Nieves-Chinchilla, T. 2012, ApJ, 748, 109, doi: 10.1088/0004-637X/748/2/109

Isavnin, A. 2016, ApJ, 833, 267, doi: 10.3847/1538-4357/833/2/267

Kilpua, E., Koskinen, H. E. J., & Pulkkinen, T. I. 2017a, Living Reviews in Solar Physics, 14, 5, doi: 10.1007/s41116-017-0009-6

Kilpua, E. K. J., Balogh, A., von Steiger, R., & Liu, Y. D. 2017b, SSRv, 212, 1271, doi: 10.1007/s11214-017-0411-3

Kilpua, E. K. J., Jian, L. K., Li, Y., Luhmann, J. G., & Russell, C. T. 2011, Journal of Atmospheric and Solar-Terrestrial Physics, 73, 1228, doi: 10.1016/j.jastp.2010.10.012

Lee, C. O., Hara, T., Halekas, J. S., et al. 2017, Journal of Geophysical Research (Space Physics), 122, 2768, doi: 10.1002/2016JA023495

Lepping, R. P., Jones, J. A., & Burlaga, L. F. 1990, J. Geophys. Res., 95, 11957, doi: 10.1029/JA095iA08p11957

Lugaz, N., Downs, C., Shibata, K., et al. 2011, ApJ, 738, 127, doi: 10.1088/0004-637X/738/2/127

Lugaz, N., Farrugia, C. J., Winslow, R. M., et al. 2018, ApJL, 864, L7, doi: 10.3847/2041-8213/aad9f4

Lugaz, N., Temmer, M., Wang, Y., & Farrugia, C. J. 2017, SoPh, 292, 64, doi: 10.1007/s11207-017-1091-6

Lugaz, N., Salman, T. M., Zhuang, B., et al. 2022, ApJ (in press)

Lynch, B. J., Zurbuchen, T. H., Fisk, L. A., & Antiochos, S. K. 2003, Journal of Geophysical Research (Space Physics), 108, 1239, doi: 10.1029/2002JA009591

Manchester, W., Kilpua, E. K. J., Liu, Y. D., et al. 2017, SSRv, 212, 1159, doi: 10.1007/s11214-017-0394-0

Marubashi, K., & Cho, K. S. 2015, Sun and Geosphere, 10, 119

Marubashi, K., & Lepping, R. P. 2007, Annales Geophysicae, 25, 2453, doi: 10.5194/angeo-25-2453-2007

Matsui, H., Farrugia, C. J., & Torbert, R. B. 2002, Journal of Geophysical Research (Space Physics), 107, 1355, doi: 10.1029/2002JA009251

Moran, P. A. P. 1950, Oxford University Press - Biometrika, 37, 17, doi: 10.2307/2332142

Möstl, C., Farrugia, C. J., Kilpua, E. K. J., et al. 2012, ApJ, 758, 10, doi: 10.1088/0004-637X/758/1/10

Mulligan, T., & Russell, C. T. 2001, J. Geophys. Res., 106, 10581, doi: 10.1029/2000JA900170

Mulligan, T., Russell, C. T., Anderson, B. J., et al. 1999, J. Geophys. Res., 104, 28217, doi: 10.1029/1999JA900215

Nieves-Chinchilla, T., Colaninno, R., Vourlidas, A., et al. 2012, Journal of Geophysical Research (Space Physics), 117, A06106, doi: 10.1029/2011JA017243

Nieves-Chinchilla, T., Jian, L. K., Balmaceda, L., et al. 2019, SoPh, 294, 89, doi: 10.1007/s11207-019-1477-8

Nieves-Chinchilla, T., Linton, M. G., Hidalgo, M. A., & Vourlidas, A. 2018a, ApJ, 861, 139, doi: 10.3847/1538-4357/aac951

Nieves-Chinchilla, T., Linton, M. G., Hidalgo, M. A., et al. 2016, ApJ, 823, 27, doi: 10.3847/0004-637X/823/1/27

Nieves-Chinchilla, T., Vourlidas, A., Raymond, J. C., et al. 2018b, SoPh, 293, 25, doi: 10.1007/s11207-018-1247-z

Odstrčil, D., Dryer, M., & Smith, Z. 1996, J. Geophys. Res., 101, 19973, doi: 10.1029/96JA00479

Owens, M. J. 2020, SoPh, 295, 148, doi: 10.1007/s11207-020-01721-0

Owens, M. J., Lockwood, M., & Barnard, L. A. 2017, Scientific Reports, 7, 4152, doi: 10.1038/s41598-017-04546-3

Pal, S., Nandy, D., Srivastava, N., Gopalswamy, N., & Panda, S. 2018, ApJ, 865, 4, doi: 10.3847/1538-4357/aada10

Palmerio, E., Nieves-Chinchilla, T., Kilpua, E. K. J., et al. 2021, Journal of Geophysical Research (Space Physics), 126, e2021JA029770, doi: 10.1029/2021JA029770

Patsourakos, S., Vourlidas, A., Török, T., et al. 2020, SSRv, 216, 131, doi: 10.1007/s11214-020-00757-9

Pomoell, J., & Poedts, S. 2018, Journal of Space Weather and Space Climate, 8, A35, doi: 10.1051/swsc/2018020

Richardson, I. G. 2018, Living Reviews in Solar Physics, 15, 1, doi: 10.1007/s41116-017-0011-z

Scolini, C., Dasso, S., Rodriguez, L., Zhukov, A. N., & Poedts, S. 2021a, A&A, 649, A69, doi: 10.1051/0004-6361/202040226

Scolini, C., Rodriguez, L., Mierla, M., Pomoell, J., & Poedts, S. 2019, A&A, 626, A122, doi: 10.1051/0004-6361/201935053

Scolini, C., Winslow, R. M., Lugaz, N., & Poedts, S. 2021b, ApJL, 916, L15, doi: 10.3847/2041-8213/ac0d58

Scolini, C., Winslow, R. M., Lugaz, N., et al. 2022, ApJ, 927, 102, doi: 10.3847/1538-4357/ac3e60

Sharma, R., & Cid, C. 2020, A&A, 642, A233, doi: 10.1051/0004-6361/202038927

Slavin, J. A., Middleton, H. R., Raines, J. M., et al. 2019, Journal of Geophysical Research (Space Physics), 124, 6613, doi: 10.1029/2019JA026892

Tsurutani, B. T., Gonzalez, W. D., Tang, F., & Lee, Y. T. 1992, Geophys. Res. Lett., 19, 73, doi: 10.1029/91GL02783

Verbeke, C., Pomoell, J., & Poedts, S. 2019, A&A, 627, A111, doi: 10.1051/0004-6361/201834702

Vourlidas, A. 2014, Plasma Physics and Controlled Fusion, 56, 064001, doi: 10.1088/0741-3335/56/6/064001

Wang, Y., Shen, C., Wang, S., & Ye, P. 2004, SoPh, 222, 329, doi: 10.1023/B:SOLA.0000043576.21942.aa

Webb, D. F., & Howard, T. A. 2012, Living Reviews in Solar Physics, 9, 3, doi: 10.12942/lrsp-2012-3

Weiss, A. J., Möstl, C., Davies, E. E., et al. 2021, A&A, 656, A13, doi: 10.1051/0004-6361/202140919

Wicks, R. T., Owens, M. J., & Horbury, T. S. 2010, SoPh, 262, 191, doi: 10.1007/s11207-010-9509-4

Winslow, R. M., Lugaz, N., Philpott, L. C., et al. 2015, Journal of Geophysical Research (Space Physics), 120, 6101, doi: 10.1002/2015JA021200

Winslow, R. M., Lugaz, N., Scolini, C., & Galvin, A. B. 2021a, ApJ, 916, 94, doi: 10.3847/1538-4357/ac0821

Winslow, R. M., Scolini, C., Lugaz, N., & Galvin, A. B. 2021b, ApJ, 916, 40, doi: 10.3847/1538-4357/ac0439

Winslow, R. M., Lugaz, N., Schwadron, N. A., et al. 2016, Journal of Geophysical Research (Space Physics), 121, 6092, doi: 10.1002/2015JA022307

Winslow, R. M., Lugaz, N., Philpott, L., et al. 2020, ApJ, 889, 184, doi: 10.3847/1538-4357/ab6170

Yashiro, S., Gopalswamy, N., Michalek, G., et al. 2004, Journal of Geophysical Research (Space Physics), 109, A07105, doi: 10.1029/2003JA010282

Zhang, J., Richardson, I. G., Webb, D. F., et al. 2007, Journal of Geophysical Research (Space Physics), 112, A10102, doi: 10.1029/2007JA012321